Master's Thesis

3D printed Ni Functionalized Polymer Derived Ceramics as CO_2 Methanation Catalysts

Carried out at the

Institute of Materials Chemistry

Faculty of Technical Chemistry

TU Wien

under the supervision of

Associate Prof. Dipl.-Ing. Dr.in techn. Karin Föttinger

By

Deborah Judith Steiner, BSc.

[redacted]

Vienna, 01.06.2023

Eidesstattliche Erklärung

Ich erkläre an Eides statt, dass die vorliegende Arbeit nach den anerkannten Grundsätzen für wissenschaftliche Abhandlungen von mir selbstständig erstellt wurde. Alle verwendeten Hilfsmittel, insbesondere die zugrunde gelegte Literatur, sind in dieser Arbeit genannt und aufgelistet. Die aus den Quellen wörtlich entnommenen Stellen sind als solche kenntlich gemacht.

Abstract

CO_2 capturing and utilisation is a promising strategy to reduce atmospheric CO_2 emissions, particularly in the context of 'Power to Fuel', where CO_2 is converted into fuels and chemicals using hydrogen sourced from excess renewable energy. The present thesis focuses on the production of highly active and selective heterogeneous catalysts for the conversion of CO_2 to methane. The catalytic activity of a material is not only determined by the active phase, but also by the characteristics and properties of the support. In this study, nickel catalysts supported on polymer derived SiOC ceramics were investigated. These ceramics offer a high specific surface area for the dispersion of nickel particles, as well as the ability to create complex shapes using 3D printing technology. The nickel functionalisation was achieved via an impregnation method and in-situ functionalisation by incorporating nickel particles into the preceramic precursor solution before additive manufacturing.

The resulting catalysts were characterised using XRD for phase analysis and calculation of crystallite size, N_2 physisorption measurements for the determination of the specific surface area, as well as CO_2 TPD measurements to estimate the basicity of the material and CO adsorption experiments to gain information on the accessibility of the nickel particles.

In addition to investigating the impact of varying nickel loadings on catalytic activity, the effect of La-modification of the support was addressed. Due to the increased basicity of the support, the potential improvement of the interaction of the catalyst with CO_2 was assessed. Furthermore, optimization of catalyst geometry was achieved through the preparation of impregnated gyroid structures. The catalysts prepared via the impregnation route, with a nickel loading of 15 wt%, achieved a maximum CO_2 conversion of 75 % at a reaction temperature of 400 °C. However, the active sites of the in-situ functionalised catalysts were found to be inaccessible, necessitating the implementation of post-pyrolysis treatments. An oxidizing treatment ultimately resulted in a maximum CO_2 conversion of 64 % at a reaction temperature of 400 °C.

Zusammenfassung

Eine vielversprechende Strategie zur Verringerung der CO_2-Emissionen ist die Nutzung von CO_2, insbesondere im Zusammenhang mit dem "Power to Fuel" Konzept, bei dem CO_2 unter Verwendung von Wasserstoff, der aus überschüssiger erneuerbarer Energie gewonnen wird, in Kraftstoffe und Chemikalien umgewandelt wird. Die vorliegende Arbeit befasst sich mit der Herstellung hochaktiver und selektiver heterogener Katalysatoren für die Umwandlung von CO_2 in Methan. Die katalytische Aktivität eines Materials wird nicht nur durch die aktive Phase, sondern auch durch die Merkmale und Eigenschaften des Trägers bestimmt. In dieser Diplomarbeit wurden Nickelkatalysatoren auf Polymer-abgeleiteten SiOC-Keramiken untersucht. Diese Keramiken bieten eine hohe spezifische Oberfläche für die Dispersion der Nickelpartikel sowie die Möglichkeit, mit Hilfe der 3D-Drucktechnologie komplexe Formen zu erzeugen. Die Nickelfunktionalisierung erfolgte über eine Imprägnier-Methode und eine In-situ-Funktionalisierung durch Einbringung von Nickelpartikeln in die präkeramische Precursor Lösung vor der additiven Fertigung.

Die resultierenden Katalysatoren wurden mittels XRD zur Phasenanalyse und Berechnung der Kristallitgröße, N_2-Physisorption Messungen zur Bestimmung der spezifischen Oberfläche, sowie CO_2-TPD-Messungen zur Abschätzung der Basizität des Materials und CO-Adsorptionsexperimente zur Gewinnung von Informationen über die Zugänglichkeit der Nickelpartikel charakterisiert.

Neben der Untersuchung der Auswirkungen unterschiedlicher Nickelbeladungen auf die katalytische Aktivität wurde auch der Effekt der La-Modifikation des Trägers untersucht. Dadurch sollte die potenzielle Verbesserung der Wechselwirkung des Katalysators mit CO_2 durch die Erhöhung der Basizität des Trägers beurteilt werden. Darüber hinaus wurde die Optimierung der Katalysatorgeometrie durch die Herstellung imprägnierter gyroider Strukturen erreicht. Die über den Imprägnierungsweg hergestellten Katalysatoren mit einer Nickelbeladung von 15 Gew.-% erreichten eine maximale CO_2-Umwandlung von 75 % bei einer Reaktionstemperatur von 400 °C. Im Gegensatz dazu erwiesen sich die aktiven Stellen der in-situ funktionalisierten Katalysatoren als unzugänglich. Eine oxidierende Behandlung nach der Pyrolyse führte schließlich zu einem maximalen CO_2-Umsatz von 64 % bei einer Reaktionstemperatur von 400 °C.

Danksagung

Als allererstes möchte ich meiner Betreuerin Karin Föttinger danken, für ihre fachkundige Betreuung, die vielen anregenden Diskussionen und wertvollen Impulse, die sie mir während meiner Arbeit gegeben hat. Danke für deine Ermutigungen und dein Engagement, die nicht nur meine Forschung bereichert, sondern auch meinen Horizont erweitert haben.

Ein besonderes Dankeschön auch an Johannes Eßmeister, der immer ein offenes Ohr für alle möglichen Probleme hatte. Seine Bereitschaft, mir bei all meinen Fragen zu helfen, war unbezahlbar. Er hat nicht nur beim 3D-Drucken, sondern auch bei den unterschiedlichsten Messungen tatkräftig an meiner Seite gestanden. Seine Expertise und Hilfsbereitschaft haben den Fortschritt meiner Arbeit erheblich unterstützt.

Bei Thomas Konegger möchte ich mich für die großzügige Bereitstellung der Laborkapazitäten bedanken, die es mir ermöglicht haben, nicht nur die Katalysatoren herzustellen, sondern auch am Test-Stand die katalytische Aktivität zu messen.

Ein großer Dank gebührt auch der Österreichischen Forschungsförderungsgesellschaft FFG, die dieses Projekt finanziell unterstützt haben (POLYCAT3D, Projektnummer 27577950).

Ebenfalls möchte ich mich bei den Mitgliedern der Forschungsgruppe Technische Katalyse bedanken, die mich stets unterstützt haben und wertvolles Feedback zu meinen Präsentationen gegeben haben.

Zu guter Letzt möchte ich meiner Familie und meinen Freunden danken, die mich während dieser Zeit immer unterstützt haben, sei es emotional oder auf andere Weise. Eure Liebe, Ermutigung und Geduld haben mir Kraft gegeben und mich dazu inspiriert, meine Ziele zu verfolgen.

Ich bin zutiefst dankbar für die Unterstützung aller genannter Personen und deren wertvollen Beiträge während meiner Masterarbeit. Diese Mitwirkung hat nicht nur zu meinem persönlichen Wachstum beigetragen, sondern auch dazu, dass meine Forschung erfolgreich war.

Table of Contents

1 Introduction

The increase of greenhouse gases (GHGs) in the atmosphere produces a positive radiative forcing of the climate system by reducing the outgoing infrared radiation, resulting in a warming of the surface temperature. Additionally, thermal expansion of warmer seawater leads to rising sea levels. Hence climate change induced by global warming is one of the significant threats to modern civilization. In total, about 82 % of the total greenhouse gases (GHGs) is covered by CO_2.[1] The reason for the continuous rise in atmospheric CO_2 levels is undoubtedly the utilization of carbon-rich fossil fuels such as coal, oil, and natural gas. The increase of the CO_2 concentration since pre-industrial times is evidenced by multiple studies and rose from 280 ppm before the industrial revolution to 405 ppm in 2017.[2–4] Organisations like the International Energy Agency (IEA) or the Intergovernmental Panel on Climate Change (IPCC) introduced the discussion of future emission trajectories based on different scenarios. The two-degree scenario was proposed to ensure no more than 2 ˚C of warming above pre-industrial levels, where total anthropogenic CO_2 emissions need to be reduced to less than 20 Gt_{CO2} per year by 2050. Additionally, further reductions to near-zero or even net-negative emissions by the end of the century are necessary. If anthropogenic emissions are allowed to increase to 60 Gt_{CO2} per year by 2050, a warming of approximately 6 ˚C will result, also known as the six degree scenario.[5]

Due to the severe consequences of global warming, a lot of research is being conducted regarding measures for the reduction of CO_2 emissions. Concerning the controlling of CO_2 emissions five broadly defined technical options are being explored: Energy choices, energy efficiency, CO_2 capture, CO_2 sequestration, and CO_2 utilization.[6,7] The latter is getting more and more attention not only from the scientific community, but also from industry.

The ever-increasing demand of natural gas goes hand in hand with the continuous rise of the atmospheric CO_2 emissions. Therefore, a non-fossil-based, sustainable source of methane (CH_4) is needed. A promising strategy is the sustainable production of "synthetic" natural gas (SNG) through the conversion of CO_2 by using hydrogen (H_2) produced from renewable energy sources. In this context latest research focuses on the development of catalysts for electrochemical, photocatalytic, or thermal catalytic reduction of CO_2 which exhibit high activity, selectivity and long-term stability.[1,8] One rather simple chemical route to produce SNG from CO_2 is through CO_2 methanation, which was first proposed by the French Chemist Paul Sabatier in 1902, equation (1).[9]

$$CO_2(g) + 4H_2(g) \leftrightarrow CH_4(g) + 2H_2O(g);\ \Delta H^\circ_{298K} = -165\ \text{kJ mol}^{-1} \quad (1)$$

In principle, the hydrogenation of CO_2 to methane is thermodynamically favourable at low temperatures. However, the reaction is kinetically hindered since the reduction of CO_2 is an eight-electron process. Additionally, the CH_4 selectivity is reduced at higher temperatures (about 450 ˚C)

due to the production of CO via the reverse water-gas-shift reaction. For that reason, there is a great demand for a highly active catalyst to overcome the kinetic barrier at low temperatures.[10] A typical methanation catalyst consists of an active phase which is finely dispersed on a support. Various noble and transition metals have been investigated and the following order of decreasing activity was found: Ru >> Fe > Ni > Co > Rh > Pd > Pt, Ir. The most promising transition metal for industrial application proved to be Ni, owing to its low cost, abundance, and relatively high activity.[11] Supplementary, the support plays a key role in enhancing the performance of a heterogeneous catalyst, affecting the metal-support interaction as well as the metal dispersion. The most investigated catalyst supports until now are metal oxides, activated carbon, composite oxides and SiC, Al_2O_3 being the most common one.[12] This work utilizes the relatively new concept of polymer derived ceramics (PDCs) as a support for CO_2 methanation catalysts. PDCs were first discovered in the 1960s and recent research trends and progress combines the functionalization of PDCs with 3D printing for the realization of complex shapes.[13] Thus, the focus of this work is the Ni functionalization of PDCs and the improvement of the catalytic activity of the printed components in combination with the characterisation of the material.

2 Literature Review

2.1 CO_2 Conversion

The very low Gibbs free energy of carbon dioxide (-394 kJ mol^{-1}), the high carbon bond strength and the very strong double bonds with oxygen atoms make CO_2 an incredibly stable molecule. Consequently, the first challenge of CO_2 conversion is to overcome the stability of said molecule. The juxtaposition of a carbon atom in isolation, which has four electrons available to form bonds, to the carbon atom in CO_2 shows, that all four electrons are tightly gripped by the oxygen atoms. Hence, this bond needs to be loosened to convert CO_2 to valuable chemicals and fuels.[14,15] Given the focus of this work being the comprehension and implementation of the Sabatier reaction, the following sections will elucidate the principal aspects of the hydrogenation of CO_2 toward CH_4, associated reaction mechanisms, effects of catalyst, as well as support.

2.1.1 CO_2 Hydrogenation

In principle the main products of catalytic CO_2 hydrogenation are methane, methanol, DME and hydrocarbons, as depicted in Figure 1. Complementary, this graphic points out, that different reactions are catalysed depending on the applied catalyst. Numerous scientists devoted their research to the utilization of CO_2, a widely available waste resource, as a cheap raw material. The combination of hydrogen production from electrolysis using excess renewable energy from wind and solar power with CO_2 capture and chemical conversion result in the sustainable production of chemicals and fuels without depending on fossil raw materials. This concept is also known as “Power to Fuel”.[16,17]

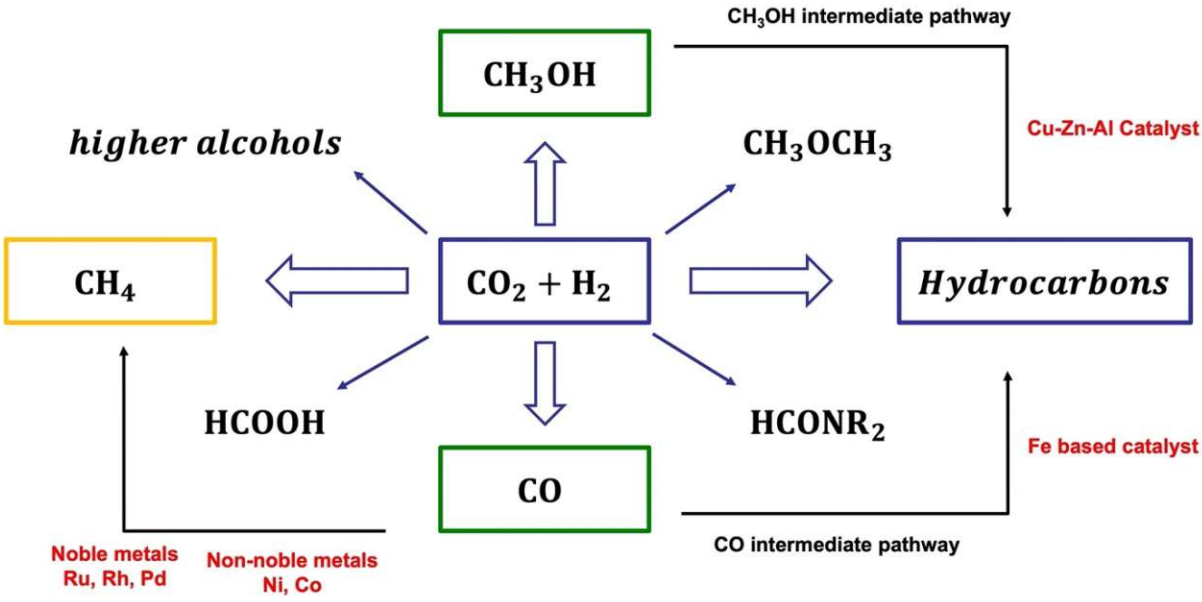

Figure 1: CO_2 conversion to chemicals and fuels through hydrogenation, adapted from [16] and [17].

Alongside the employed catalyst another crucial aspect when determining the desired product molecule is the H_2/CO_2 ratio. Studies have shown that a H_2/CO_2 ratio of 4 in combination with non-noble metal catalysts like Ni or Co, or noble metal catalysts favour the Sabatier reaction, which results in CH_4 formation. Since this reaction is the focus of this thesis, detailed elucidations of the reaction mechanisms will be discussed in the following section. In contrast, methanol is the main product of CO_2 hydrogenation when Cu catalysts are employed and a H_2/CO_2 ratio of 3:1 is realised. Owing to its extensive applications as solvent, energy source and chemical feedstocks methanol is one of the main raw materials in chemical and petrochemical industries. For that reason, the production of methane and methanol from CO_2 have gained considerable attention, also in context with the "Power to Fuel" concept.[16,17]

2.1.2 Sabatier Reaction: Methanation Mechanisms

Equation 1 describes the Sabatier reaction, which is known to be an exothermic reaction ($\Delta G_{298K} = -130{,}8\ \mathrm{kJ\ mol^{-1}}$). Nonetheless, the reduction of the fully oxidized carbon to CH_4 has substantial kinetic constraints since the process involves eight-electrons. Hence appropriate catalysts are needed to achieve a high CH_4 selectivity.[18] The topic of suitable catalysts will be fully discussed in the following chapter, whereas the focus of this chapter lies on the exploration of the reaction mechanism regarding the CO_2 methanation.

The occurrence of side-reactions is highly probable during methanation. Gao et al. summarized the possible reactions involved in the methanation of carbon oxides, given in Table 1 from theoretical thermodynamic analyses.[19] R1 and R2 represent the normal methanation reactions. In addition, the key role of water becomes apparent, especially when considering R5, the water gas-shift reaction. Moreover, the calculation of the equilibrium constants at varying temperatures showed, that all

reactions are favoured at low temperatures (< 400 °C). However, when increasing the temperature above 450 °C, the production of CO by-product is favoured, due to the reverse water gas shift reaction. [16,19]

Table 1: Possible reactions involved int the methanation of carbon oxides, adapted from Gao et al. [19]

Reaction No.	Reaction Formula	ΔH_{298}(kJ mol^{-1})	Reaction type
R1	$CO + 3H_2 \leftrightarrow CH_4 + H_2O$	-206,1	CO methanation
R2	$CO_2 + 4H_2 \leftrightarrow CH_4 + 2H_2O$	-165,0	CO_2 methanation
R3	$2CO + 2H_2 \leftrightarrow CH_4 + CO_2$	-247,3	Inversed methane CO_2 reforming
R4	$2CO \leftrightarrow C + CO_2$	-172,4	Boudouard reaction
R5	$CO + H_2O \leftrightarrow CO_2 + H_2$	-41,2	Water gas shift
R6	$CH_4 \leftrightarrow C + 3H_2$	74,8	Methane cracking
R7	$CO + H_2 \leftrightarrow C + H_2O$	-131,3	Carbon monoxide reduction
R8	$CO_2 + 2H_2 \leftrightarrow C + 2H_2O$	-90,1	Carbon dioxide reduction

Generally, two groups of mechanisms of the CO_2 methanation are discussed in literature. Firstly, the associated adsorption of CO_2 and secondly, the dissociated reaction scheme. Concisely, in an associative scheme the CO_2 adsorption occurs associatively and the reaction with adsorbed hydrogen atoms is followed by the formation of oxygenates which are hydrogenated to methane in successive steps. The distinguishing feature in this sequence is that no CO intermediate is formed. In contrast, the dissociative scheme is characterised by the CO_2 dissociation initially into carbonyl (CO) and an oxygen atom. Subsequently, the carbonyl is hydrogenated step by step in the same mechanisms as CO methanation proceeds where methane is ultimately formed. Consolidated, it is still a matter of dispute which mechanism is correct, given that different studies conducted their experiments with varied catalysts (support as well as active sites) and reaction conditions.[18,20]

Summarized the major challenge when determining the reaction mechanism is the identification of the elementary steps. Precisely, answers to the following three questions are needed: (1) What are the intermediates? (2) What are the elementary steps, especially the rate-determining steps that lead to the intermediates? (3) What are the active sites?[20] Hereinafter, the proposed obstacles are elucidated regarding the prior mentioned reaction schemes.

2.1.2.1 The CO_2 associative methanation

In situ Fourier transform infrared spectroscopy (FTIR) is broadly utilized to gain insight on the reaction mechanism of the CO_2 methanation.[21,22] The FTIR spectra revealed that CO_2 from the gas

phase adsorbs as carbonate CO_{3ad} on the support and gets hydrogenated into several oxygenates such as bicarbonate HCO_{3ad}, formate $HCOO_{ad}$, and formyl CHO_{ad}.[18] The latter being the most discussed intermediate in literature, where the connection between formate and CH_4 formation was found from infrared data and mass spectroscopy results.[20,22] In addition, investigations by Westermann et al. concluded formate as the precursor for both CH_4 and CO.[23] Furthermore, the gaseous dihydrogen split is proposed to occur on the reduced metal particles. Hence, the metal-support interface is suggested to be the location of the active sites, where adatoms H_{ad} are transferred to the support.[18] Concluding, researchers engaging in investigations regarding the associative CO_2 mechanisms claim that the CH_4 selectivity is ultimately determined by the competition between C-O bond scission and H_xCO species and their hydrogenation reactions.[24] Moreover, the binding of H_xCO species should be strengthened by the metal/oxide interface to facilitate the C-O bond splitting to obtain methane with high selectivity.[18]

2.1.2.2 The CO_2 dissociative scheme

In the CO_2 dissociative scheme carbon dioxide from the gas phase adsorbs and splits into carbonyl and an oxygen atom. According to scientists supporting the dissociative mechanism, the C-O bond breaking barrier is reduced particularly at low-coordinated sites (i.e., step and kink sites), where the direct CO_2 dissociation can be achieved. Hence, the intermediates in this reaction pathway are CO_{ad}, O_{ad} and surface carbon C_{ad}. The subsequent reaction mechanism, once the adsorbed CO_{ad} has been formed, is closely related to the Fischer-Tropsch mechanism.[18]

2.2 Suitable Heterogeneous Catalysts for CO_2 Methanation

Over the last century a great number of methanation catalysts have been developed, which have been discussed and reviewed in literature. Typical methanation catalysts are composed of active metal particles finely dispersed on a support. Particularly, the active metal phase has been extensively investigated for its catalytic activity, both in noble metals (Ru, Rh, Pt and Pd) and non-noble metals (Ni, Fe, Mo and Co).[4] Besides the catalytic activity, the methane selectivity is of great importance due to the large number of possible reactions described in Table 1. Generally, the respective metal catalysts show the following activity and selectivity:

Activity: Ru >> Fe > Ni > Co > Rh > Pd > Pt > Ir [4,10,12]

Selectivity: Pd > Pt > Ir > Ni > Rh > Co > Fe > Ru [10,25]

Nevertheless, it is crucial to mention that the given order is only a generalised trend which can vary depending on different metal support interactions.[10]

The high activity at low temperatures and low metal loadings favours the use of noble metals. Ruthenium, in particular, is known to have the best overall catalytic performance. Yet noble metal-based catalysts are rarely employed for industrial applications owing to their high cost and low availability.[26] Therefore, non-noble metal catalysts, with the focus being on nickel, are the most

widely studied catalysts, offering comparable activity at much lower cost. A summary of properties of the most commonly used catalysts is given in Table 2. Furthermore, evaluations of Ru and Ni catalytic data shows that higher temperatures are required when using Ni catalysts to achieve a maximum methane yield. Consequently, one of the main disadvantages of Ni catalysts is their short lifetime due to carbon deposition leading to blocked pores and a deactivated catalyst.[10,27] This problematic is discussed in the following sections.

Table 2: Juxtaposition of the characteristics of the most common methanation catalysts, adapted from Kuznecova et al. [27]

Methanation Catalyst	Advantages	Disadvantages
Ru (ruthenium)	- Most active metal - High methane yield at low temperatures - Higher stability in CO and CO_2 methanation process than Ni	- About 600 times more expensive than Ni[28,29] (cost dated 19.05.2023)
Fe (iron)	- Chemical activity higher than Ni - Long lifetime – environmentally friendly - Lower price compared to Ni - Application at high temperatures possible (700 – 950 °C)	- Extremely low selectivity
Ni (nickel)	- High activity and selectivity - Low cost and widely available	- Short catalyst lifetime - High sensitivity for sulfur poisoning
Co (cobalt)	- Similar activity to Ni - No induction period required	- Higher cost than Ni
Mo (molybdenum)	- High methane selectivity - Sulfur tolerant properties	- Low activity

2.3 Ni catalysts for CO_2 methanation

The comparison of the most investigated heterogenous catalysts given in Table 2 results that nickel combines cost-effectiveness and efficiency regarding the CO_2 methanation reaction; hence it is the most frequently employed catalyst for this particular reaction. Nonetheless, there are some challenges associated with the employment of Ni in industrial catalytic processes including carbon deposition, sintering of Ni particles due to the susceptibility of Ni to agglomeration, and severe sulfur poisoning during SNG production leading to a low stability of the catalyst. Consequently, Ni catalysts have a short lifetime and low reusability. Additionally, carbon deposition and metal sintering result in catalyst deactivation. To counter these phenomena, various strategies have been developed such as the use of a second metal promoter, which can improve CO_2 methanation through a synergistic effect and the ability to resist carbon deposition. Further, the choice of catalyst support helps with the improvement of the metal dispersion, the provision of a high specific surface area, and the anchoring will reduce Ni particle sintering.[30]

2.3.1 Deactivation of Ni Catalysts

Catalyst deactivation is a complex process that involves various mechanisms, including poisoning, coking and sintering.[31] Coking is the accumulation of carbonaceous deposits on the catalyst surface, which can block the active sites and reduce the surface area available for the reaction. It is a severe problem in dry reforming of methane, but is negligible in CO_2 methanation. Sintering is another possible deactivation process which occurs when high reaction temperatures rapidly promote the agglomeration and coalescence of small metal crystallites which reduces the surface area and active sites available for the reaction. Different ways to slow down Ni sintering have been established, including the increase of the metal-support-interaction, adding promotors or adopting improved preparation methods. Poisoning on the other hand occurs due to impurities in the feed gas, sulfur compounds (H_2S or thiophene (C_4H_4S) being the major contaminations. Besides blocking the active sites, sulfur poisoning also accelerates the sintering and oxidizing of Ni^0 particles. Yet, improvement of the sulfur resistant Ni methanation catalysts is still in need of more in depth research.[12, 29–31]

2.3.2 Role of the support

The catalytic activity of the catalyst is heavily impacted by the characteristics and properties of the support, which can significantly contribute to the overall efficiency of the process. The dispersion of the active phase, for instance, can be improved substantially with the enhancement of metal-support interactions. Since CO_2 is an acidic molecule the modification of the surface chemistry to more basic properties improve the CO_2 coverage of the catalyst, which results in an enhancement of the CO_2 methanation performance at lower temperatures. Concluding, the selection of the right support material and its subsequent modification can be of tremendous importance when seeking to increase the efficiency of the process.[34]

Various materials suitable for supporting nickel as the active metal have been studied and reviewed. Metal oxides such as ZrO_2, Al_2O_3 and TiO_2 are the most common catalyst supports due to their excellent stability for the deposition of well-dispersed active metal. Lanthanide metals like CeO_2 or La_2O_3 on the other hand provide an abundant number of basic sites as well as more defects for CO_2 adsorption and activation, hence they are considered as the most promising potential supports. Additionally, the participation of graphene and boron materials in the modification of the electron structure can affect the dispersion of the active metal and the nature of adsorbed species formed in the reaction.[35]

Nickel catalysts are usually prepared via different impregnation methods. Metal oxide supports with high surface areas are advantageous to disperse nickel nanoparticles. Prior to methanation reaction usually a reducing pretreatment is performed to turn Ni^{2+} species to Ni^0 nanoparticles.[32] Further, the strong metal-support interaction (SMSI) between nickel nanoparticles and reducible oxide supports may also have an impact on the surface morphology of supported nickel-based catalysts. The SMSI effect can result in encapsulation of metallic nickel by an oxide overlayer from the support. Pre-

reducing the support prior the introduction of nickel species during preparation is one option to avoid this phenomenon.[36] Concluding, in addition to improving dispersion, the interaction between nickel and support can reconstruct exposed surface facets. Moreover, during the synthesis of nickel-based catalysts it is crucial to consider the SMSI effect, which may result in the encapsulation of active sites by an oxide overlayer.[32]

Complementary to the structural effects described in the previous paragraph, the manipulation of catalyst basicity is an important tool to control the CO_2 adsorption behaviour. Studies have shown that the number of basic sites is positively correlated with the apparent catalytic activity. Further, the addition of La has been found to greatly increase the activity of Ni/γ-Al_2O_3, as the support composed of lanthanum and aluminium contains more basic sites, which leads to easier CO_2 adsorption. Yet, the relationship between the strength of basic sites and kinetics of CO_2 activation is still being debated. A method commonly used to detect the basicity of a catalyst is temperature-programmed desorption of CO_2 (CO_2-TPD). Based on the desorption temperature, basic sites can be categorized as weak, medium, or strong, which are attributed to surface OH-groups, metal-oxygen pairs, and coordinatively unsaturated O_2-ions.[32] Muyoyama et al. investigated the correlation between support basicity and CO_2 methanation activity using a series of supported nickel-based catalysts. They found that among the catalysts with varying supports, Ni/Y_2O_3 exhibited the best activity and desorbed the largest amount of CO_2 at around 400°C during CO_2-TPD. Conversely, Ni/La_2O_3 with the poorest activity desorbed CO_2 mainly at temperatures over 400°C, indicating that strong basic sites are not favourable for CO_2 methanation.[37] Further, oxygen vacancies on the catalyst surface play a crucial role in the activation of CO_2 molecules. H_2 can partially reduce the catalyst surface and form oxygen vacancies that easily react with CO_2 at elevated temperatures. Aziz et al. showed that the high activity of Ni/MSN (mesostructured silica nanoparticles) is due in part to the formation of surface oxygen vacancies, which facilitate the formation of methane from carbon species adsorbed on the MSN support.[38]

Further, the mechanism of the CO_2 methanation reaction can also be altered by the choice of support. Generally, the reaction requires two types of active sites: While the H_2 dissociation and CO methanation usually happen on metallic Ni^0 nanoparticles, metallic Ni^0 sites or the metal-support interface are responsible for CO_2 adsorption and activation. Hence, new reaction pathways are possible with increasing CO_2 adsorption capacity of the support. In addition, it is possible that reducible supports containing surface oxygen vacancies during the reaction can boost CO_2 activation. Nonetheless, as stated in section 2.1.2, the exact reaction mechanism is still being debated in literature and may be support-dependent. [32]

This thesis introduces the novel concept of using polymer derived ceramics (PDCs) as a catalyst support. This relatively new approach aims to improve not only the metal-support interaction but also to increase the specific surface area and metal dispersion. To reduce Ni sintering during the

methanation reaction, a support with high thermal conductivity is beneficial, as it can rapidly dissipate the reaction heat. PDCs prepared with additive manufacturing (AM) have proven to be a viable alternative to conventional supports and will be the focus of the following section.

2.4 Additive Manufacturing of Polymer Derived Ceramics and the Utilisation as Catalyst Support

Ceramics made from preceramic polymer (PCP) precursors are a promising alternative to traditional ceramic synthesis and manufacturing methods. PCPs are a type of silicon-based polymers that can provide ceramics with a tailored chemical composition and precisely defined nanostructure through crosslinking and subsequent thermal treatment (which involves curing and thermolysis processes) under specific conditions. Depending on the type of polymer used, it is possible to produce different ceramic materials; for instance, PSOs (polysiloxanes) can be used to create SiOC ceramics, while polycarbosiloxanes can produce SiC ceramics. Generally, silicon-based PCPs are commonly referred to as "organosilicon polymers". [39–41]

The composition and distribution of phases, as well as the microstructure of the final ceramic, are influenced by the molecular structure and type of PCP used. Thus, the main obstacle is to create appropriate PCPs through chemical synthesis. Ideally, a PCP should have appropriate solubility, melting temperature, and rheological properties for shaping. The material should also be designed with functional groups that allow for crosslinking to maintain its shape when exposed to heat. It should possess a non-linear molecular structure to prevent low molecular weight ingredients from evaporating during polymer pyrolysis, and a high ceramic yield.[42]

This thesis explores the use of SiOC ceramics derived from PSO as a catalyst support. Polysiloxanes are a important type of PCP resins having the typical chemical structure $–[Si(CH_3)_2\text{-}O]-$ and exist in the form of chains, ladders, and 3D network polymers.[42] The degree of 3-dimensional crosslinking can be modified by adjusting the end groups of the PSO. Non-linear polysilsesquioxanes have been found to be a fitting PCP for the intended use of additive manufacturing. These compounds are recognized by the formula $–[RSi\text{-}O_{1.5}]_n-$ (where R can denote hydrogen, an organic aryl group, or an organic alkyl group).[39]

The process of converting polymeric precursors into PDCs goes through several main steps that can affect their compositions and properties. These steps include:

- Crosslinking of the monomers using a catalyst (at temperatures ranging from 25 to 400°C)
- Pyrolysis of the highly-crosslinked preceramic materials to form an infusible organic/inorganic network (at temperatures ranging from 400 to 1400°C)
- Phase separation into crystallites at higher temperatures (between 1000 to 2000°C)

The crosslinking of polysiloxanes is a crucial process that increases the ceramic yield and maintains the bulk shape during ceramization. Using a suitable catalyst, such as a photoinitiator, the photo-crosslinking of polysiloxanes can even occur at room temperatures.[43]

As this thesis centers on the production of 3D printed Ni catalysts, photocrosslinking is the chosen technique for additive manufacturing. This method relies on stereolithography and enables the creation of complex structures with a high level of flexibility, without being restricted to the structures created using traditional ceramic methods. In stereolithography, the process involves exposing the thin two-dimensional layers of a photocurable resin, which consists of photopolymerizable monomers like acrylates, to laser irradiation in a successive manner. This causes the liquid layers to solidify on top of each other until a three-dimensional part is completely built. In general, photopolymerization is a process in which long-chain macromolecules are formed through the continuous reaction of monomers in the presence of light. This chain reaction is initiated by a photoinitiator, which absorbs photons from the exposed light to form reactive species that are essential for polymerization. The reactive species then react with the functional groups of monomers within the liquid resin, generating further reactive species. As the reaction chain increases, solid polymer structures are formed. The rate and depth of polymerization are influenced by the intensity and wavelength of light. [44,45]

The properties of ceramics derived from polymeric siloxanes can be modified by changing the temperature at which they are pyrolyzed. Pyrolysis between 400-800°C results in the creation of porous and surface-rich materials known as ceramers, where the polymer is only partially converted to ceramic. Careful control of the pyrolytic conversion at intermediate temperatures is critical in altering the surface's hydrophobicity, producing micro- and mesopores, and generating highly porous components.[46]

2.5 Current state of the project

During her master's thesis conducted in the research group for "Technical Catalysis", Eva Szoldatits explored the catalytic properties of functionalized polymer-derived ceramics. She developed, optimized, and produced Ni impregnated polymer derived SiOC powders. Through her work, the author was able to achieve significant conversions of CO_2 to methane. However, to ensure that Ni particles are well distributed and accessible on printed components, improvements to the PDC support are necessary, given its low specific surface area and the challenges involved in impregnating.[47] To control the porous morphology of the 3D printed components, one approach is to take advantage of the phase separation phenomenon. To create a hierarchical porosity, a miscible photoresin composed of acrylate monomers and pre-ceramic precursors is polymerized. Once polymerized using stereolithography, the three-dimensional component is defined by a bicontinuous structure of organic polymer and pre-ceramic polymer. Upon pyrolysis of the printed object a nanoporous structure with a high specific surface area is achieved.[48] To be used as a catalyst support,

Anna-Maria Fuchsberger, from the project team “Advanced Ceramics” of the Institute for Chemical Technologies and Analytics, developed a phase separating resin by incorporating Silres-MK, a polysilsesquioxane, as the PCP and TMPTMA (trimethylolpropane trimethacrylate) as the acrylate monomer. Due to the poor solubility between PCPs and acrylate monomers, teraethylorthosilicate (TEOS) was introduced as a solubilizing agent to the system. This approach enabled achievement of high specific surface areas of the printed components.[49]

On the other hand, the objective of Johannes Eßmeister’s dissertation thesis, conducted in the project team “Advanced Ceramics” of the Institute for Chemical Technologies and Analytics, was to in-situ modify PDCs for the CO_2 methanation reaction. Therefore, one purpose of this thesis is to compare the two distinct approaches, impregnation, and in-situ functionalization, for phase-separating polymer-derived ceramics.

3 Aim of this work

Reducing CO_2 emissions and exploring alternative energy sources are two of the greatest challenges of our time. Among the potential solutions to this crisis, the CO_2 methanation reaction has emerged as a promising option. This reaction involves the reduction of CO_2 to CH_4 using H_2, but due to the high kinetic barrier, a highly active and selective catalyst is required. Nickel is the most common catalyst for this reaction; however, its use is limited by complex deactivation mechanisms such as nickel particle sintering, carbon deposition, or sulfur poisoning.

To address these challenges and enhance catalyst stability, an appropriate catalyst support must be chosen. The main scope of this thesis was the preparation and investigation of nickel catalysts supported on polymer derived SiOC.

The objectives of this work were:

- To develop an impregnation technique for 3D-printed components that yields high CO_2 conversions with high selectivity.
- To compare the catalytic activity of the developed impregnation technique with in-situ functionalized components.
- To optimize the catalyst geometry for improved performance.
- To characterize the resulting catalysts through:
    - Measurement of the catalytic performance of the CO_2 methanation reaction.
    - Utilization of powder diffraction methods and scanning electron microscope.
    - Investigation of temperature-programmed desorption of CO_2.
    - Examination of CO adsorption in the IR-vacuum cell.
    - Analysis of N_2 adsorption and desorption.

4 Materials and Methods

4.1 Preparation of Ni functionalized Catalysts

4.1.1 Stereolithographic Preparation of Polymer-Derived Ceramic Components

Before stereolithographic manufacturing of the green bodies, the phase-separating resin was prepared. First, the pre-ceramic polymer precursor Silres-MK, a polysilsesquioxane, was dissolved in TPM. To accomplish the appropriate composition for the phase separating resin, a 1:1 solution of MK:TPM was created by dissolving the MK powder in an equivalent weight of TMP in a round flask. To attain a yield of roughly 1 g of printed components, a total of 40 g of resin was prepared. Anna-Maria Fuchsberger fine-tuned the proportion of PCP, acrylate, and solubilizer, finding that the most favourable outcome was reached with a mixture of 44 wt% MK:TPM, 44 wt% TMPTMA, and 12 wt% TEOS. The aforementioned chemicals were dissolved in a beaker until a clear solution with low viscosity was obtained. Then 0,0275 wt% of the colorant Sudan Orange was added as a light absorber for the following printing process. Once a clear solution was achieved, 1 wt% of the photo-initiator BAPO was added under the exclusion of blue light and dissolved in an ultra-sonic bath for ten minutes. Table 3 summarizes the materials used for the printing process.

Table 3: Summary of the chemicals used for the preparation of the phase separating resin

Material	Function	Abbreviation	Provider
Tri(propyleneglycol)-methyl ether	Solvent	TPM	Formlabs
Trimethylolpropane-trimethacrylate, 85 %	Photosensitive acrylate	TMPTMA, 85 %	Sigma-Aldrich
Tetraethyl orthosilicate, 98 %	Solubilizing Agent	TEOS, 98 %	Sigma-Aldrich
Polymethyl silsesquioxane	Preceramic Polymer	PSO; Silres MK	Wacker
Sudan Orange G, 85 %	Light absorber	-	Sigma-Aldrich
Genorad-BAPO	Photo-initiator	-	Rahn AG

The vat-based photopolymerization of both simple and complex geometries was achieved by using unmodified resins and a 3D desktop printer (Anycubic Photon Mono 4K). The light exposure was provided by a monochrome LCD screen with LEDs at a 405 nm wavelength. The resin tank was equipped with an FEP foil (ELEGOO, FEP 2.0 Release Film Liner, 0.127 nm thickness), a non-stick foil that allowed for gentle detachment of each cured layer. The printing platform was covered with adhesive tape, and a primer layer (photosensitive acrylate mixed with 1wt% BAPO) was applied, which was cured under UV-light for 1 minute. The printing platform was calibrated before pouring the defoamed resin into the tank and the printing process was started by following the printing

parameters given in Table 4. After printing, the cured components were carefully detached from the printing platform using a razor blade.

Table 4: Parameters for the 3D printing process on the desktop printer

Parameters for unmodified resin	
Exposure time (s)	25
Bottom exposure time (s)	40
Exposure intensity (mW cm^{-2})	2
Bottom layer count	5
Layer hight (µm)	25
Light-off delay (s)	0,5
Bottom lift speed (mm min^{-1})	60
Lifting Speed (mm min^{-1})	60
Bottom retract speed (mm min^{-1})	180
Retract speed (mm min^{-1})	180

Once the printing process was complete, excess resin was removed by placing the components in TPM. For more complex structures, an ultrasonic bath with TPM was required to remove the surplus resin. Prior to pyrolysis, the printed components were dried under argon atmosphere for 12 hours at 130°C. Then the green bodies were pyrolyzed under argon atmosphere in a three-zone split tubular furnace equipped with an aluminium oxide tube (HZS 12/600, Carbolite Gero). The argon gas-flow was adjusted to 0,35 L min^{-1} and the oven was heated in several heating steps to ensure sufficient burnout and the formation of porous structures, where the holding temperatures were determined by Anna-Maria Fuchsberger. An overview of the fabrication process for the 3D printed components is shown in Figure 2 and the pyrolysis temperature profile is depicted in Figure 3.

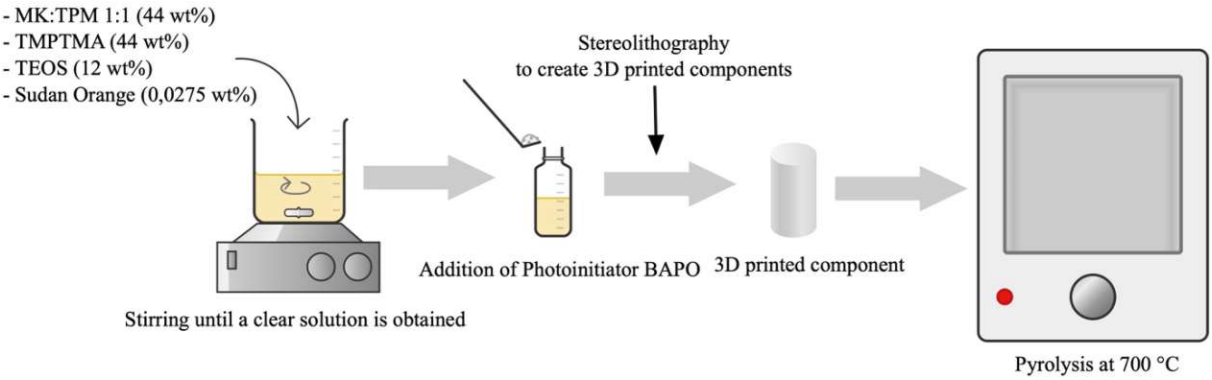

Figure 2: 3D Printing Process: Preparation of the Phase-Separating Resin; Addition of the Photo-initiator; Stereolithography; Pyrolysis at 700 °C under argon atmosphere

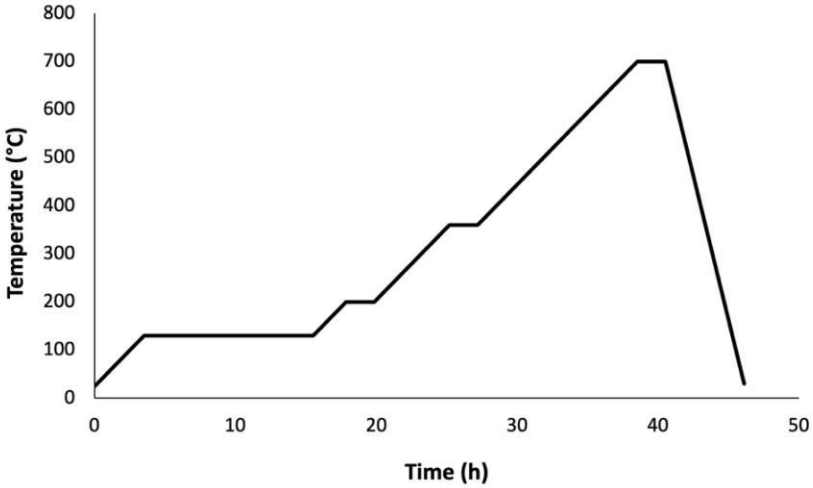

Figure 3: Pyrolysis temperature profile

4.1.2 Impregnation Functionalization

To achieve a nickel concentration of 5 wt%, 10 wt%, or 15 wt% on the printed component, the appropriate amount of nickel nitrate hexahydrate (M = 290,79 g mol^{-1}) was dissolved in about 5 mL of THF. Once a clear solution was obtained, the cylinders were added to the solution. To evaluate the effect of a higher nickel loading on the impregnation technique, two distinct approaches were employed for the preparation of catalysts containing 10 wt% nickel. The first method involved impregnating the cylinders with two consecutive steps of 5 wt% nickel, whereby the cylinders were dried overnight at 110 °C between the impregnation steps. In the second approach, a separate batch of catalysts was prepared with 10 wt% nickel through a single impregnation step.

To investigate the impact of different nickel precursors and solvents, a batch of catalysts was created with varying conditions. Specifically, nickel acetylacetonate was dissolved in toluene. The catalysts made with these different methods are distinguished later on with the labels "NiN" for those made with the nickel nitrate precursor and "NiA" for those made with the nickel acetylacetonate precursor. Table 5 provides an overview on the different impregnation methods for various 3D-printed supports.

Table 5: Overview of the precursors and solvents used in different impregnation methods

Method	Support	Precursor	Solvent
1	Unmodified PSO	Nickel nitrate hexahydrate	THF
2	Unmodified PSO	Nickel acetylacetonate	Toluene
3	La-modified PSO	Nickel nitrate hexahydrate	THF
4	La-modified PSO	Nickel nitrate hexahydrate	Ethanol

Next, the round flask was placed in an ultrasonic bath at 40 °C for 4 hours. Afterwards, the solvent was removed using a rotary evaporator while slowly rotating, heating the water bath to 40 °C and adjusting the pressure accordingly. The impregnated cylinders were dried at 110°C for 12 hours and then calcinated at 440°C for 4 hours under argon atmosphere. Figure 4 shows a graphical overview of the impregnation process.

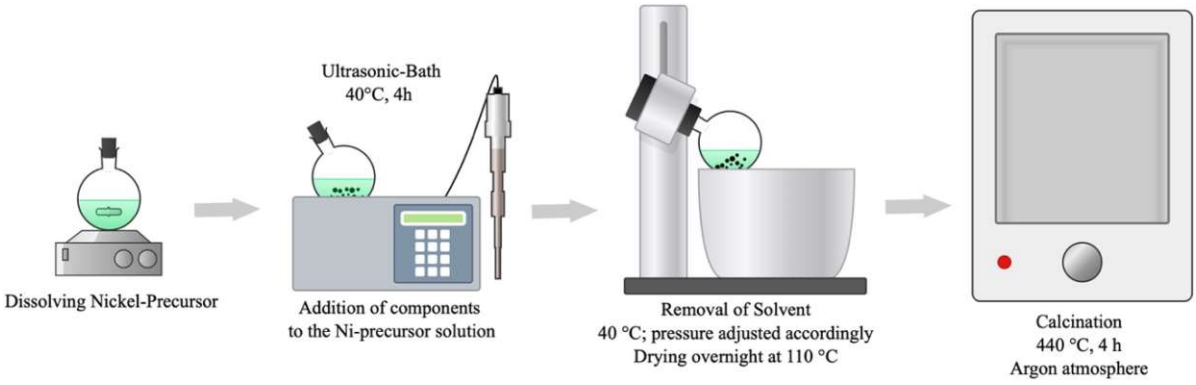

Figure 4: Overview of the Impregnation Process

4.1.3 In-Situ Functionalization

Johannes Eßmeister was responsible for preparing the in-situ functionalized components. To prepare the metal-modified resin, a water-free environment was crucial, so the glassware used for combining the chemicals was dried overnight at 110 °C, then transferred to a nitrogen-filled glove box. Metal acetylacetonates were also stored and handled under nitrogen. An overview of the metal acetylacetonates employed for in-situ functionalisation is given in Table 6. Tetrahydrofuran (THF, Roth, 99,5 %, 10 ppm H_2O) was used as a solvent for the polymer-modification reaction with $Ni(acac)_2$. Propionic acid (PA, Merck, 99%) was employed for $La(acac)_3$.

Table 6: Overview of used metal acetylacetonates for the in-situ functionalization

Metal Acetylacetonate	Synonym	Provider
Nickel(II) acetylacetonate – $Ni(acac)_2$	Nickel (II) 2,4-pentanedionate, 95 %	Alfa Aesar
Lanthanum(III) acetylacetonate hydrate – $La(acac)_3$	2,4-Pentanedione lanthanum hydrate, 99,9 %	Alfa Aesar

4.2 Determination of the Catalytic Performance

The catalytic activity was measured using a self-assembled fixed bed steel reactor[47] with an inner diameter of 6 mm, operating at atmospheric pressure. Three different scenarios were tested for filling the reactor with catalyst:

- In the first option, 0,5 g of 3D printed cylinders were placed into the reactor, with quartz wool at both ends.
- In the second scenario, the cylinders were milled using a vibrating mill (Retsch MM 400) with a ZrO_2 inlet at a frequency of 30 s^{-1} to generate a particle size of less than 180 µm. For the reaction, 0,5 g of catalyst powder was mixed with 0,5 g of Al_2O_3 as a filler material.
- In the last scenario, 0,5 g of 3D printed gyroid structures that fit exactly into the reactor were stacked upon each other.

The catalysts were prepared for the catalytic reaction by pretreating them with a gas flow of 25 mL/min containing 10 vol% H_2 in He at 400°C for a duration of 4 hours. After the pretreatment, the gas feed composition was changed to the reaction conditions with a gas flow of 25 mL/min consisting of 10 vol% CO_2, 40 vol% H_2, and 50 vol% He. The resulting outlet gas compositions were analysed after being cooled down to 300°C and following the temperature profile depicted in Figure 6 using an Inficon Micro GC Fusion. The analysis was conducted using a method developed by Eva Szoldatits, which was initially calibrated for a gas flow of 50 mL/min in her work but was subsequently adjusted for a gas flow of 25 mL/min using a reference catalyst.

Equations (2) and (3) show the calculations of the CO_2 conversion X_{CO2} and the selectivity to methane S_{CH4}. In these equations [X] (X = CO_2, CH_4) represents the molar fraction of component X in the outlet gas.

$$X_{CO_2} = \frac{[CO_2]_{in} - [CO_2]_{out}}{[CO_2]_{in}} \cdot 100 \quad (2)$$

$$S_{CH_4} = \frac{[CH_4]_{out}}{[CO_2]_{in} - [CO_2]_{out}} \cdot 100 \quad (3)$$

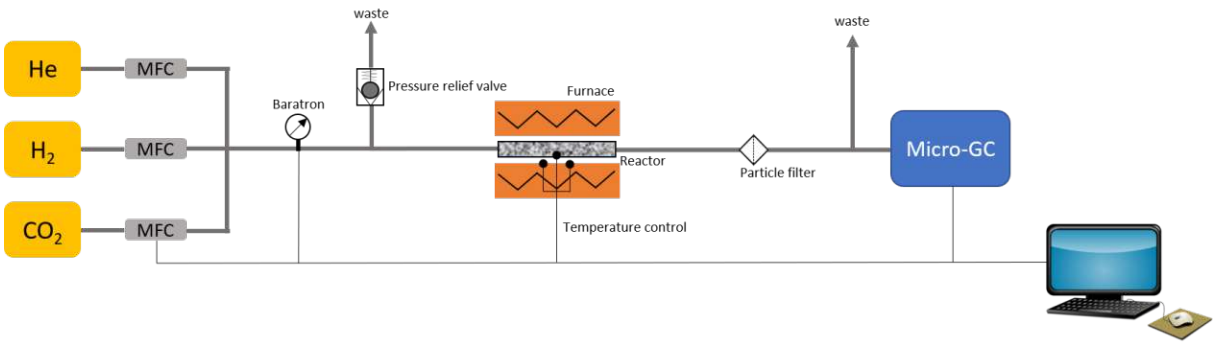

Figure 5: Setup for the CO_2 methanation measurements, adapted from [47]

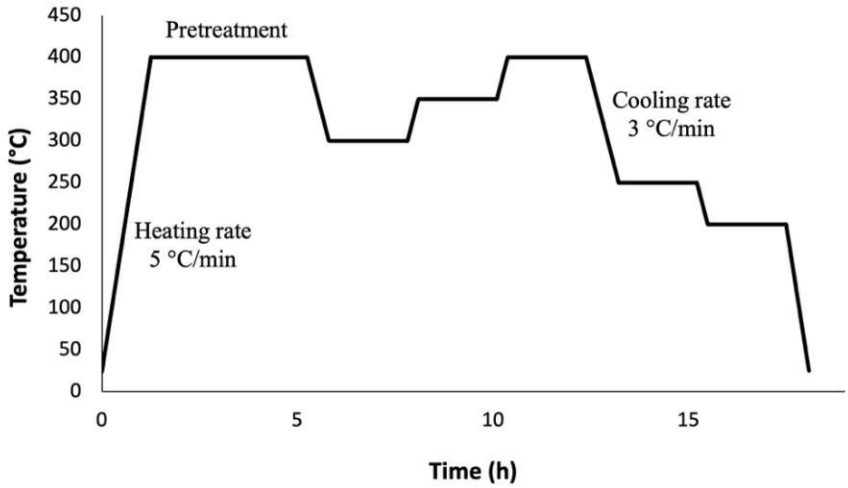

Figure 6: Temperature Profile Methanation Set Up

Table 7: Micro GC measurement setup adapted from [47]

Parameter	Module A	Module B
Column type	Mole sieve	PLOT-Q
Inject time	0 s	24 ms
Backflush time	15 s	-
Temperature injector	90 °C	90 °C
Temperature detector	70 °C	70 °C
Column pressure	30 psi	15 psi
Column temperature	60 °C	60 °C
Hold time	450 s	450 s
Sample pump	20 s	20 s

4.3 Catalyst Characterization

To gain further insight and information regarding the produced catalysts, various catalyst characterizations were performed. The methods applied are outlined in the following subchapters.

4.3.1 XRD

To determine whether the impregnated components contained a pure nickel phase, X-ray powder diffraction measurements (XRD) were conducted using a Malvern PANalytical MPD pro XRD. The parameters used were 45 kV anode, 40 mA (Cu-tube), 5-100 ° 2 theta, 2.546° active length, 35 seconds per step, and 25 minutes total duration. The diffractograms were refined using the Rietveld method, and the crystallite size was calculated using the Scherrer equation in the High Score Plus program.

4.3.2 N_2 Physisorption (BET)

The specific surface area is a crucial factor in determining the characteristics of a catalyst. To measure this, N_2 adsorption and desorption was performed at -196°C using a Micromeritics ASAP 2020 instrument and following the BET (Brunauer-Emmett-Teller) standard procedure with 5 measuring points (relative pressures between 0.05 and 0.3 p/p^0). Each sample, weighing approximately 100 mg, was degassed in vacuum at 300°C for 4 hours prior to measurement. The mesopore size was determined using BJH calculations assuming a cylindrical pore geometry.

4.3.3 Imaging

To analyse the morphology and structure of the catalyst surfaces, scanning electron microscopy (FEI Quanta 200) was employed. Images generated using a backscattered electron detector to visualize the contrast of materials and a secondary electron detector to demonstrate the morphology were compared. To gain more insight into the nickel dispersion SEM images were generated using the FEI ESEM Quanta 200 FEG microscope, which generates images with a higher resolution and higher magnifications. Additionally, a Keyence VHX-5000 light microscope was employed to compare the appearance of different samples.

4.3.4 CO_2 Temperature Programmed Desorption

To evaluate the surface basicity of the material and to study its capacity for adsorption, CO_2 temperature programmed desorption (CO_2-TPD) measurements were performed. The process involved placing quartz wool into the reaction tube, followed by adding 50 mg of sample on top and securing it with more quartz wool. The pressure was adjusted to 10^{-3} mbar after flushing with nitrogen twice. For the reducing pretreatment, the reaction tube was filled with 100 mbar H_2 and 400 mbar N_2 and heated to 400°C with a heating rate of 10 °C/min. Once the temperature reached 400°C, the gas mixture was renewed and held for one hour. Afterward, the sample was cooled in a vacuum atmosphere. When the sample reached room temperature, 50 mbar CO_2 was filled into the reaction

tube and adsorbed for 30 minutes. To remove weakly adsorbed species, vacuum was set for 15 minutes. Then the sample was heated to 450 °C with a heating rate of 5 °C/min and the desorbed species were detected using a quadrupole mass spectrometer (Balzers Prisma).

4.3.5 FTIR-Transmission Spectroscopy

To gain insight into the accessibility of the Ni particles, CO adsorption experiments were performed using an IR vacuum chamber. To prepare the sample, the cylinders were ground into a fine powder. Since the powder was black, a transparent KBr pellet had to be made. This was achieved by grinding KBr powder and compressing it of 2.5 tons. Once a transparent pellet was obtained, the catalyst powder was finely dispersed onto the KBr pellet using a brush and fixed with a pressure of about 1.5 tons. The resulting pellet was then put into the sample holder and inserted into the vacuum cell. The IR spectra were recorded via transmission using a Bruker Vertex 70 spectrometer equipped with a mercury cadmium telluride (MCT) detector. Prior to measurement, a background spectrum of the cell without the sample was measured under vacuum. Once the sample was in the cell, the vacuum was adjusted to 10^{-6} mbar. Before CO adsorption, a reducing pretreatment was necessary. This involved introducing 50 mbar of H_2 and 450 mbar of N_2 into the chamber and heating to 400 °C at a rate of 10 °C/min. Once the maximum temperature was reached, the gas mixture was renewed and held for 1 hour. The sample was then cooled to room temperature under vacuum. During the entire pretreatment, IR spectra were collected. Once the sample reached room temperature, a final spectrum was measured and used as a background for the following CO adsorption. For CO adsorption, 10 mbar of CO gas was introduced into the vacuum chamber, and IR spectra were measured every minute for 30 minutes. After adsorption, the vacuum was adjusted again. Depending on whether an IR band was still visible or not, the measurement was stopped, or the sample was heated again until the IR band vanished, indicating that the CO had desorbed.

5 Results

5.1 Impregnation Functionalisation

5.1.1 Phase Analysis and Crystallite Size

For the determination of the present crystalline phases on the functionalised SiOC support, powder diffractograms of the catalysts with varying nickel loading are presented in Figure 7. Owing to its amorphous nature, SiOC is not revealed in the X-ray diffraction pattern. Nevertheless, a pure nickel phase was identified, with relatively broad peaks indicating the presence of small crystallites. This assumption was confirmed by the results of the calculations of the crystallite size applying the Scherrer equation, given in Table 8. The sample impregnated with 5 wt% Ni exhibited the smallest crystallite size, with a size of 16,3 nm. Conversely, the sample impregnated with 10 wt% Ni in one step had the largest crystallite size, measuring 25,3 nm.

Table 8: Crystallite Size calculated from XRD data for catalysts with varying Ni loading

Sample Description	Crystallite Size (nm)
5NiN	16,3
10NiN 1 (two steps)	16,7
10NiN 2 (one step)	25,3
15NiN	21,2

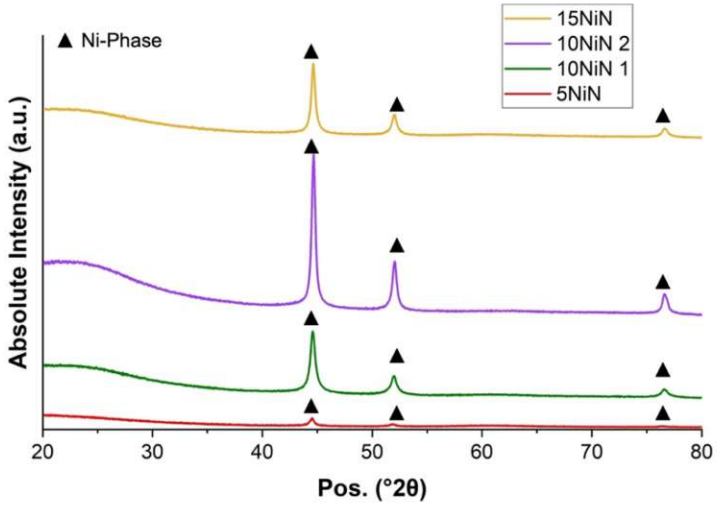

Figure 7: Powder diffraction patterns of impregnated catalysts with varying nickel loadings from 5 wt% to 15 wt%

5.1.2 Specific Surface Area and Pore Size

Figure 8 depicts the N_2-adsorption-desorption isotherms of impregnated catalysts with varying nickel loadings. The International Union of Pure and Applied Chemistry (IUPAC) has proposed a classification for pore sizes and sorption isotherms that reflects the relationship between porosity and sorption. Generally, there are six different types of adsorption isotherms. The isotherms obtained for the impregnated samples with varying nickel loading indicate a Type II isotherm, which is typical of non-porous materials with predominantly macropores. However, the small hysteresis observed suggests the presence of a limited number of mesopores.[50,51]

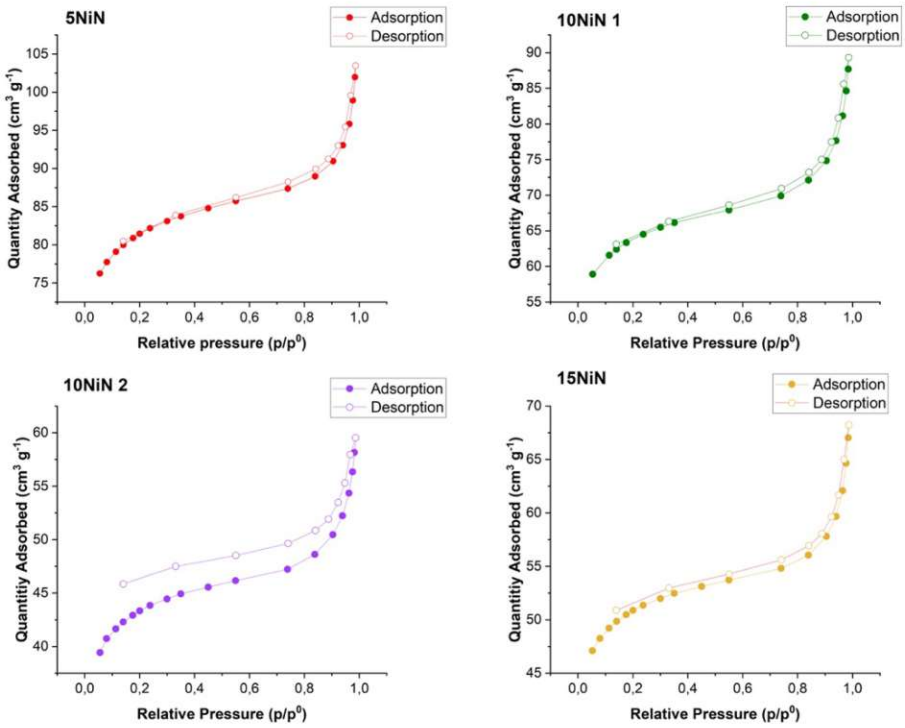

Figure 8: N_2-adsorption-desorption isotherms of impregnated catalysts with varying nickel loadings from 5 wt% to 15 wt%

Figure 9 displays the BJH pore size distribution and BET surface area of the impregnated catalysts with varying nickel loadings. Generally, mesopores are defined as pores with free diameters ranging from 2 to 50 nm[52]. Since there is no distinct peak in the mesoporous region, the average pore size cannot be obtained from the graph. An overview of the BJH average pore size is given in Table 9, where the pore size is in the range from 5,6 nm to 6,4 nm. Additionally, the BET surface area depicted in Figure 9 is similar in magnitude for all samples. Among all catalysts, the one with a 10 wt% Ni loading, impregnated in two steps, had the highest specific surface area of 196 m^2g^{-1}. Conversely, the catalyst with 10 wt% impregnated in one step had the lowest specific surface area of 134 $m^2 g^{-1}$.

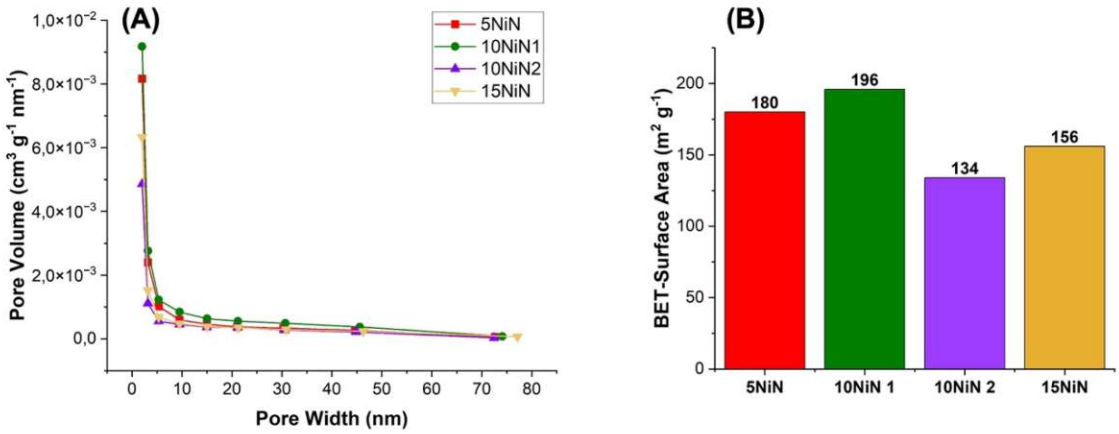

Figure 9: (A) BJH pore size distribution of the impregnated catalysts with varying Ni loadings (B) BET-surface area of impregnated samples with varying Ni loadings

Table 9: Overview of the BJH Average Pore Size of the impregnated catalysts with varying nickel loading

Sample	Average Pore Size (nm)
5NiN	5,6
10NiN 1	6,2
10NiN 2	6,4
15NiN	6,4

5.1.3 Morphology and Surface Characterisation

In Figure 10, various magnifications of the catalyst surface impregnated with 5 wt% nickel are shown. The cylinder depicted is from an early batch where the printing parameters had not yet been adjusted and exhibited large cracks. Nevertheless, EDX mapping of the magnified area marked in green showed a nickel content of 10 wt% with an error of 2 wt%. In general, the distribution of nickel particles appeared to be even.

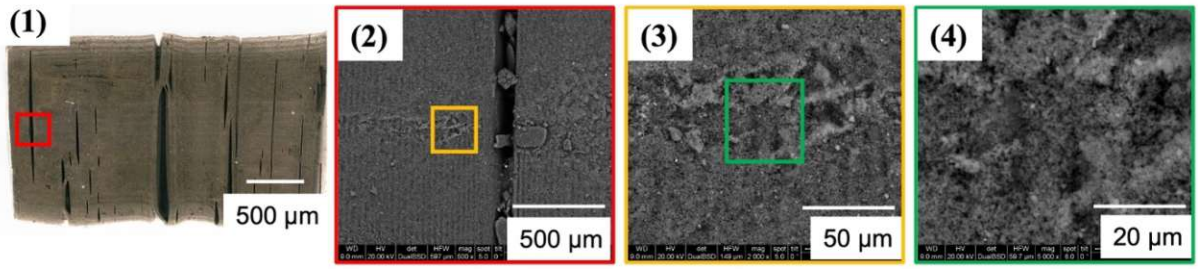

Figure 10: (1) Microscope image of a catalyst with 5 wt% nickel; (2-4) SEM images (BSE-contrast) magnifications 500x, 2000x and 5000x; EDX-mapping was performed in the area marked in green;

To gain a better understanding of the presence of nickel particles within cracks and the bulk of the cylinders, the fracture surface of a broken cylinder was investigated using SEM imaging. Figure 11 depicts the fracture surface of a cylinder with 10 wt% nickel. At 500x magnification, a band on the outside of the fracture surface was clearly visible in the secondary electron image. (2a) in Figure 11 shows the 5000x magnification of the outer edge of the fracture surface, while (2b) in Figure 11 demonstrates the 5000x magnification of the inside of the fracture surface. EDX measurements of the selected areas were performed, revealing 23 wt% nickel on the outer band with an error of 3 wt%. In contrast, EDX measurements of the inside of the fracture surface yielded only 4 wt% nickel with an error of 7 wt%.

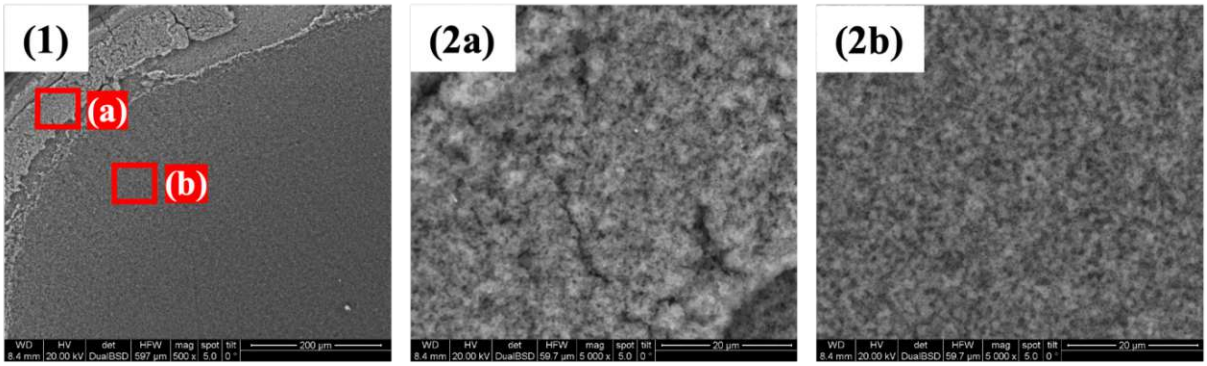

Figure 11: (1) SEM image (500x magnification, SE contrast) of the fracture surface of a catalyst with 10 wt% nickel; (2a) 5000x magnification of the outside of the fracture surface (BSE contrast); (2b) 5000x magnification of the inside of the fracture surface (BSE contrast)

Because of the poor resolution at magnifications over 10000x of the SEM images captured using the FEI Quanta 200, SEM images were taken with FEI Quanta 200 FEG for a better visualisation of the porous structure and to gain a better insight into the nickel dispersion. Figure 12 compares images of the fracture surface, representing the bulk of the material, to those of the cylinder surface. While the cylinder surface (5-8) shows a high nickel dispersion, the fracture surface (1-3) exhibits more isolated nickel particles. In Figure 12, (4) shows a secondary electron image of the fracture surface with a 50000x magnification, highlighting the porous structure of the material.

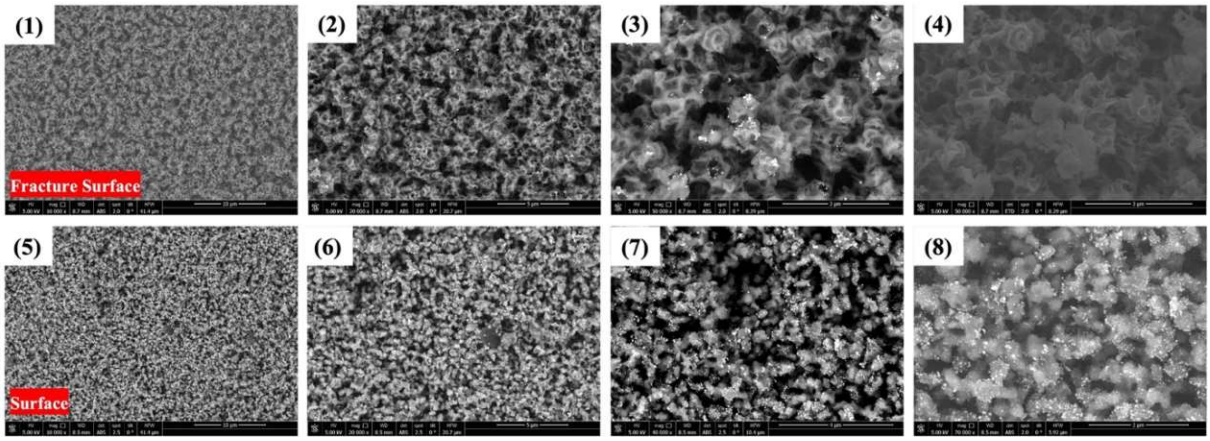

Figure 12: SEM images of the fracture surface as well as the surface of a cylinder impregnated with 15 wt% nickel (magnification from 10000x to 70000x, BSE-contrast)

5.1.4 Interaction of Catalyst with CO_2

To investigate the interaction between the catalyst and CO_2, CO_2 temperature programmed desorption (TPD) measurements were performed. Figure 13 depicts the results of the CO_2 TPD measurements, with CO_2 desorption initiation at approximately 350 °C to 400 °C. According to literature, CO_2 desorption curves can be divided into three different regions. Desorption from weak basic sites occurs between 50 °Cand 250 °C, medium basic sites desorb between 300 °Cand 600 °C, and strong basic sites feature desorption from 600 °C to 800 °C.[53] Regrettably, the investigation of CO_2 desorption in the higher temperature range was not accessible due to oven limitations. Nevertheless, the obtained results indicate the existence of medium basic sites. As anticipated, there is no substantial impact of the nickel content on CO_2 desorption.

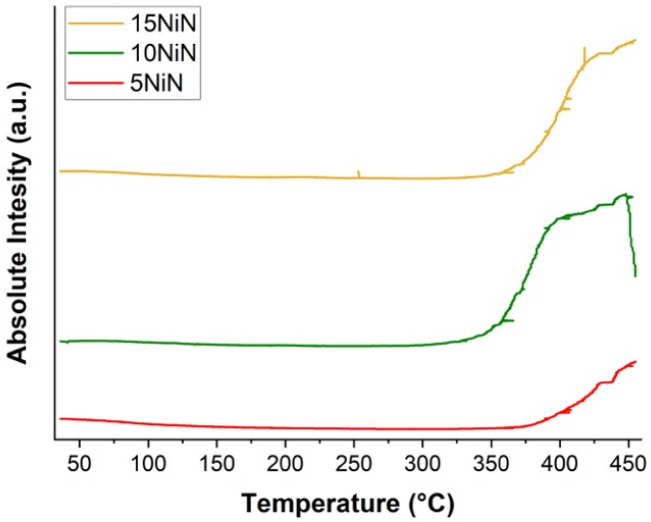

Figure 13: Results of the CO_2-TPD measurements with varying Ni-loading

5.1.5 Accessibility of Nickel

IR measurements were conducted in the vacuum cell to determine the accessibility and nature of the nickel particles. Figure 14 shows the IR spectra of CO adsorption on the catalyst with 5 wt% Ni, compared to the catalyst with 15 wt% nickel. The figure displays the temporal evolution of CO adsorption in five-minute intervals, up to a total of 20 minutes of adsorption. Additionally, it shows the IR spectra after CO adsorption, when the pressure of the IR cell was adjusted back to vacuum. The band at 2058 cm^{-1} increased during CO adsorption, but no adsorption band was visible after the vacuum was readjusted. According to literature, IR bands between 2000 and 2100 cm^{-1} indicate the stretching vibration of linearly bonded CO, rather than bridged bonded CO which occurs between 1800 cm^{-1} and 1900 cm^{-1}.[54]

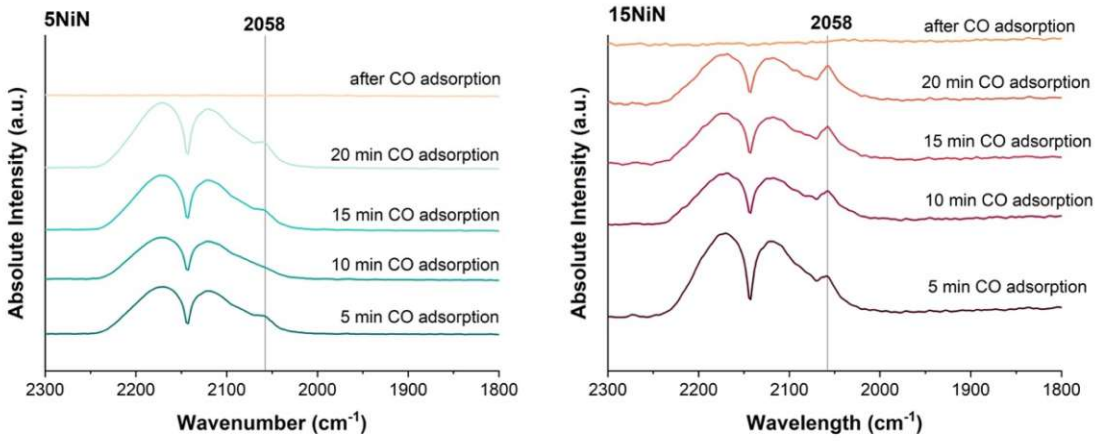

Figure 14: IR spectra of CO adsorption on catalysts with 5 wt% and 15 wt% nickel at different times of adsorption

5.1.6 Polymer Derived Ceramic Support without Functionalisation

The comparison of the powder diffractograms between the functionalized SiOC support with 5 wt% nickel and the unfunctionalized SiOC support is presented in Figure 15. It can be observed that the unfunctionalized support demonstrates solely an amorphous bump, which is typical for this type of material, and does not exhibit any crystalline phase.

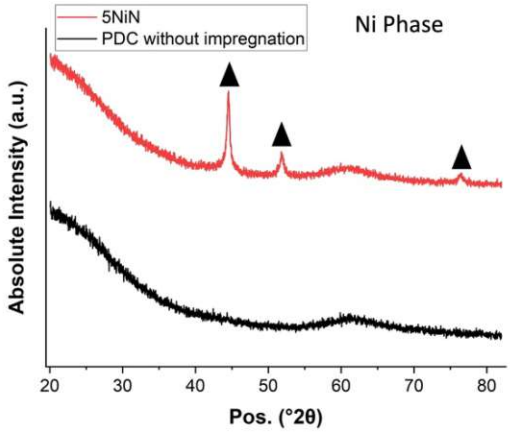

Figure 15: Powder diffraction patterns of the functionalised support with 5 wt% Nickel compared to the support without impregnation

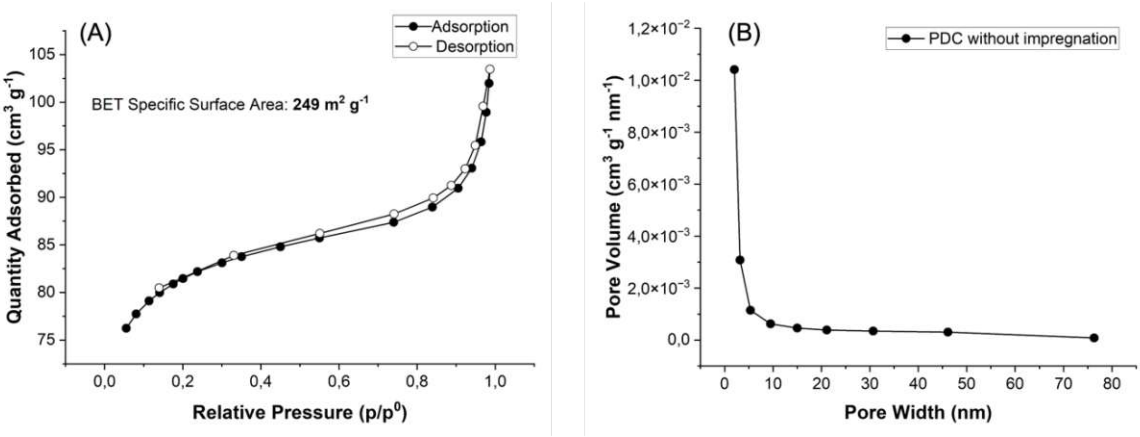

Figure 16: (A) N_2-adsorption-desorption isotherms of the support without functionalisation (B) BJH pore size distribution of the support without functionalisation.

To evaluate the impact of the nickel functionalisation on the interaction of the material with CO_2, a CO_2 TPD measurement was conducted on the unfunctionalized SiOC support. The results of the comparison clearly indicate that a lower amount of CO_2 was adsorbed, resulting in a flatter desorption curve. However, to make a more precise and conclusive statement of the basicity and strength of the interaction with CO_2, CO_2 TPD measurements at higher temperatures (such as 800 °C) would be required.

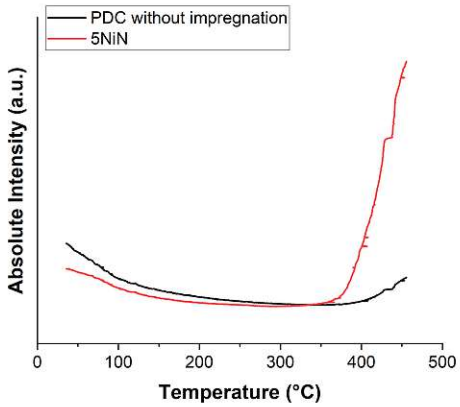

Figure 17: CO_2-TPD of the PDC without impregnation and of the functionalised catalyst with 5 wt% Ni

5.1.7 Catalytic Performance

To determine the catalytic performance, catalytic tests were conducted using the methanation set-up described in section 4.2. Figure 18 shows the results for CO_2 conversions, comparing different nickel loadings. It was observed that all samples have a similar CO_2 conversion at 400 °C; however, it was evident that catalysts with higher nickel loadings achieved higher CO_2 conversions at 300 °C and 350 °C. Specifically, the sample with 15 wt% demonstrated with 67% CO_2 conversion a 29% higher result compared to the sample with 5 wt% nickel. Moreover, the component with 10 wt% nickel impregnated in two consecutive steps resulted in a 13% higher CO_2 conversion at 350 °C compared to the sample impregnated in just one step. In general, the highest CO_2 conversion rate was achieved using the 15 wt% nickel sample, which resulted in a 75% CO_2 conversion. Additionally, the methane selectivity was 100 % for all samples at all temperatures.

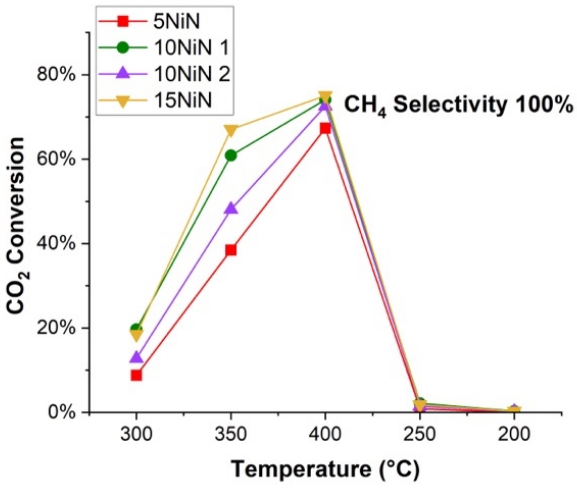

Figure 18: Comparison of the CO_2 conversion results of the impregnated catalysts with nickel loadings 5 wt%, 10 wt% and 15 wt%, where the CH_4 selectivity was 100% for all samples.

To assess the stability of the impregnated catalysts, cylinders impregnated with 5 wt% were tested under harsh conditions, specifically for 50 hours at 400 °C. The data obtained, as shown in Figure

19, demonstrate that the CO_2 conversion remained relatively stable throughout the experiment. Moreover, the CH_4 selectivity remained at 100% throughout the entire duration of the stability test.

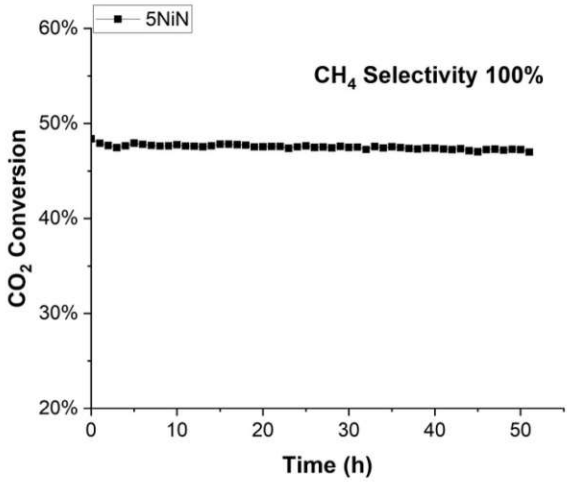

Figure 19: CO_2 conversion results of the stability test conducted at 400°C for 50 h for the catalyst with 5 wt% Ni

5.2 Nickel Precursor Variation

5.2.1 Phase Analysis and Crystallite Size

Figure 20 shows a comparison of the XRD patterns of impregnated cylinders that were prepared with different nickel precursors and solvents. The figure demonstrates the presence of a single, metallic nickel phase, and the relatively broad reflexes in both diffractograms indicate a similar crystallite size. Specifically, the SiOC support impregnated with nickel acetylacetonate and toluene as solvent exhibited a crystallite size of 15,8 nm, whereas the sample impregnated with nickel nitrate hexahydrate had a crystallite size of 16,8 nm.

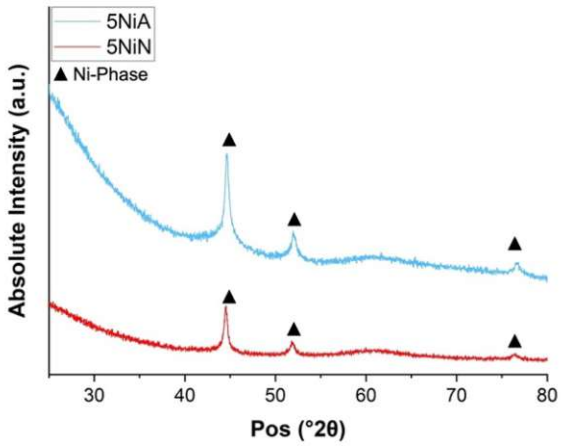

Figure 20: Comparison of powder diffraction patterns of impregnated cylinders with 5 wt% nickel and varying nickel precursor and solvent

5.2.2 Specific Surface Area and Pore Size

The N_2-adsorption-desorption-isotherms of the components impregnated with the nickel acetylacetonate precursor are presented in Figure 21 (A). The isotherms exhibit a type II pattern, indicating a non-porous or macroporous material. Notably, the hysteresis is even less pronounced compared to the components that employ nickel nitrate as the precursor. Figure 21 (B) illustrates the BJH pore size distribution of the sample coated with nickel acetylacetonate, which is comparable to the catalyst prepared with the nickel nitrate precursor. Though, the sample impregnated with nickel acetylacetonate exhibits an average pore size of 6,6 nm, which is 1 nm greater than the average pore size of the catalyst prepared with the nickel nitrate precursor.

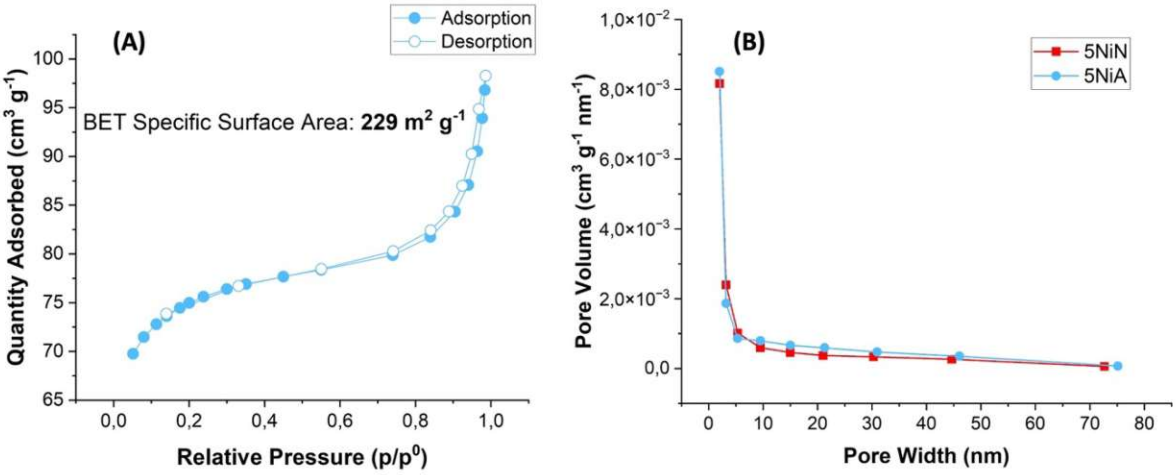

Figure 21: (A) N_2-adsorption-desorption isotherms of cylinders impregnated with 5 wt% nickel using nickel acetylacetonate as precursor; (B) BJH pore size distribution of the 5NiA sample compared to the component impregnated with the nickel nitrate precursor;

5.2.3 Morphology

The scanning electron microscope images presented in Figure 22 provide an overview of the morphology and nickel dispersion of a cylinder impregnated with the nickel acetylacetonate precursor and toluene solvent. A close examination of the catalyst surface using the BSE detector clearly revealed a poor dispersion of nickel particles. This observation was confirmed by EDX measurements of the selected areas (a) and (b), where the nickel loadings were found to be 5 wt% and 13 wt%, respectively. Moreover, it was noted that the bulk of the cylinder presents a gradient in nickel concentration. Specifically, the selected area on the outside of the fracture surface (c) exhibited a nickel content of 9 wt% nickel, while the bulk on the inside of the facture surface only contained 3 wt% nickel (d). Yet, it is crucial to note that the EDX measurements used to determine the nickel contents are susceptible to high error rates. As such, the percentages of nickel loadings in the selected areas should only be considered indicative and to further confirm the poor nickel dispersion.

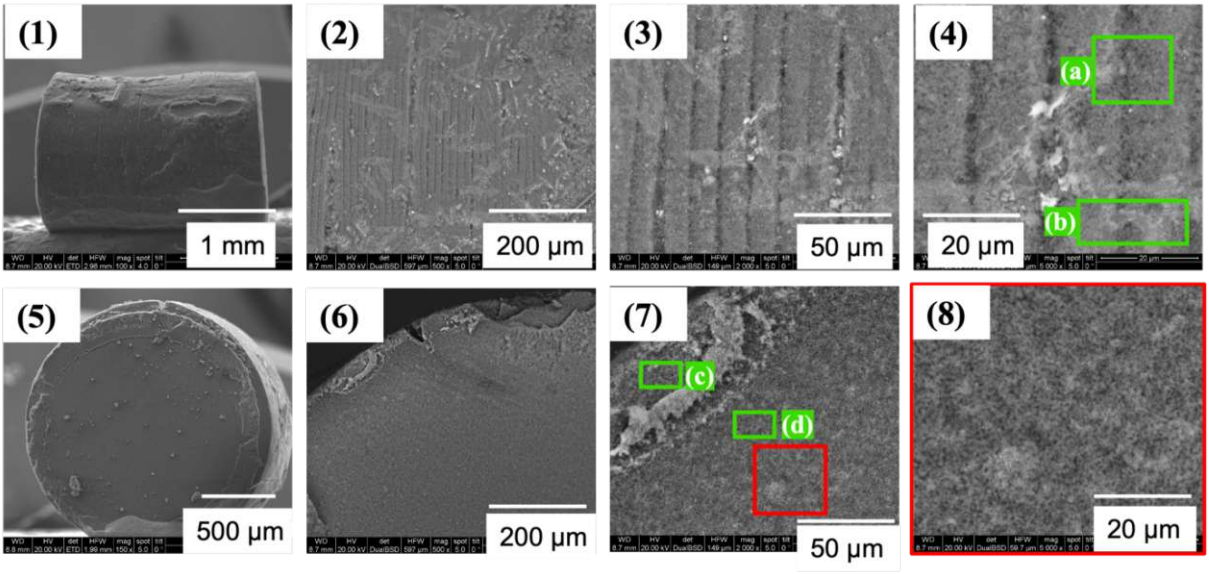

Figure 22: (1) Secondary electron image of the catalyst impregnated with nickel acetylacetonate with 100x magnification; (2-4) BSE images of the surface of the cylinder coated with nickel acetylacetonate (500x – 5000x magnification); (5) Secondary Electron image of the fracture surface of the catalyst impregnated with nickel acetylacetonate with 150x magnification; (6-8) BSE images of the fracture surface of the cylinder (500x – 5000x magnification); (a-d) mark the areas where EDX mapping was performed;

5.2.4 Catalytic Performance

Figure 23 compares the catalytic performance of the catalysts with 5 wt% nickel but varying preparation method. The results of the CO_2 conversion show that catalysts prepared with nickel acetylacetonate and toluene as solvent exhibit lower catalytic activity, particularly at 350 °C.

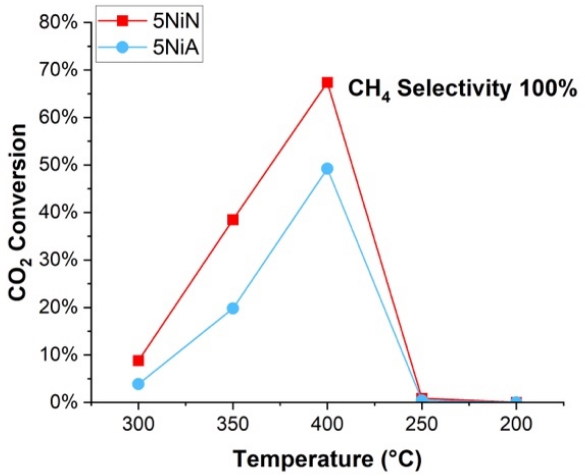

Figure 23: Comparison of the CO_2 conversion of the catalysts impregnated with nickel nitrate and THF (red) and with nickel acetylacetonate and toluene (blue)

5.3 In-situ Support Modification and Impregnation Functionalisation

5.3.1 Phase Analysis and Crystallite Size

Figure 24 compares the powder diffraction patterns of the impregnated, La-modified SiOC support. The catalyst prepared using method 4, with ethanol as the solvent for the nickel precursor, exhibits a pure metallic nickel phase. However, the catalyst prepared using method 3, with THF as the solvent also shows a NiO phase. Notably, the ethanol-prepared catalyst exhibits a larger crystallite size of 24,8 nm compared to the significantly smaller crystallite size of 7,9 nm for the THF-prepared catalyst. Moreover, the material without nickel functionalisation revealed solely an amorphous phase, which implies that lanthanum was being integrated in the SiOC matrix.

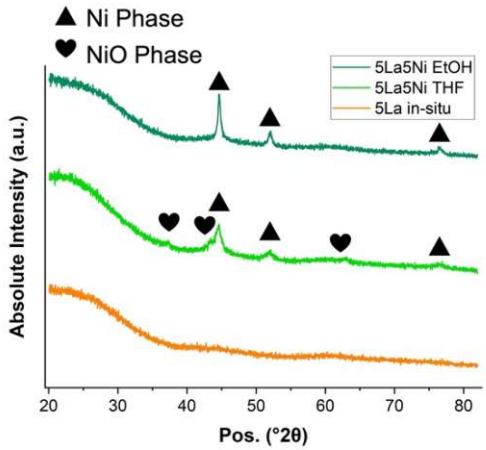

Figure 24: Comparison of powder diffraction patterns of lanthanum in-situ modified components (orange) and the nickel functionalised lanthanum in-situ modified catalysts, impregnated with 5 wt% nickel and prepared with different solvents during the impregnation process

5.3.2 Specific Surface Area and Pore Size

The N_2-adsorption isotherms of the La-modified and functionalised components are presented in Figure 25. The catalyst prepared with nickel nitrate dissolved in THF displays the characteristic type II isotherm, indicating a non-porous or macroporous material. Conversely, the catalyst in which nickel nitrate was dissolved in a more polar solvent, namely ethanol, exhibits a type IV isotherm curve with a distinct hysteresis, thereby indicating a mesoporous material.

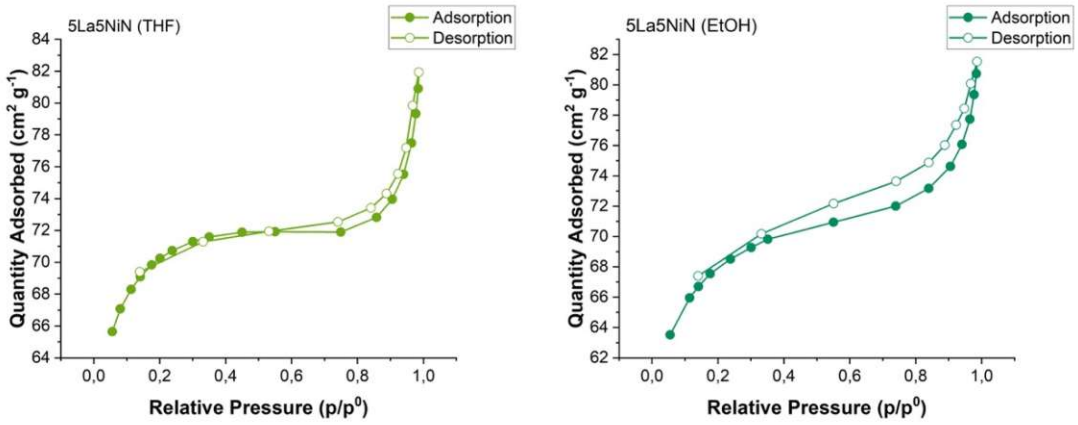

Figure 25: Comparison of the N_2-adsorption-desorption isotherms of the La-modified component functionalised with impregnation using the nickel nitrate as the precursor and varying the solvent, THF (left) and ethanol (right)

The BET-surface area of the La-modified catalysts is depicted in Figure 26 (A) and compared to that of the unmodified catalyst. It is observed that the BET surface area of the unmodified sample containing 5 wt% nickel is comparable to that of the La-modified sample with 5 wt%, when ethanol was used as the solvent. The specific surface areas were 180 m^2 g^{-1} and 175 m^2 g^{-1}, respectively. However, the sample impregnated with THF as the solvent exhibits a higher specific surface area of 213 m^2 g^{-1}, which is 38 m^2 g^{-1} greater.

In contrast, Figure 26 (B) illustrates the BJH pore size distribution of the aforementioned catalysts. This comparison reveals a similar pore size distribution, with an average BJH pore size of 5,6 nm for the unmodified catalyst and 5,7nm for the La-modified catalysts, respectively.

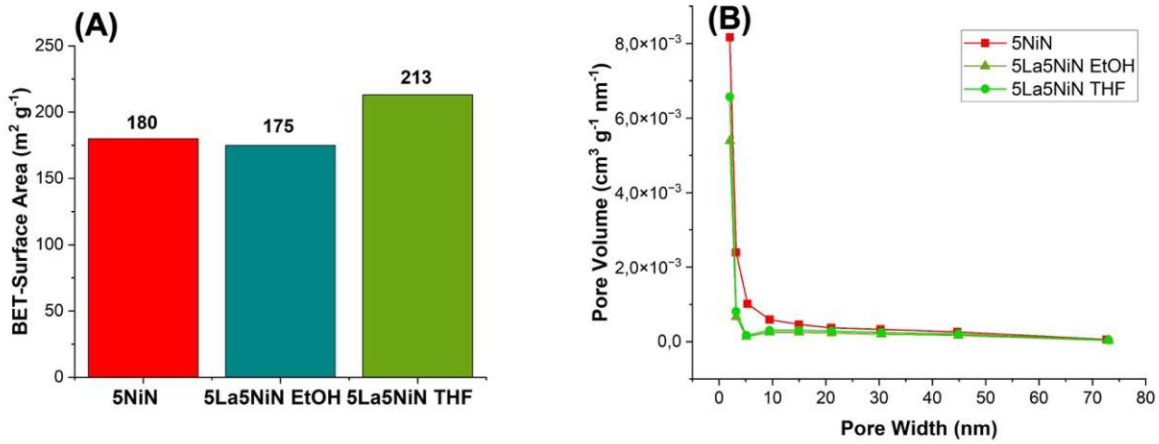

Figure 26: (A) Comparison of the BET-Surface Area of the functionalised La-modified components compared to the unmodified catalyst; (B) BJH pore Size distribution of the La-modified catalyst compared to the unmodified catalyst

5.3.3 Morphology

To demonstrate the efficacy of the impregnation of La-modified components with different solvents, 3D microscope images were created. As shown in Figure 27 (1a-b), the surface of a cylinder impregnated with nickel nitrate dissolved in THF, displays a distinct coating of metallic nickel, instead of a fine dispersion of nickel particles. In contrast, the La-modified cylinders impregnated with nickel nitrate dissolved in ethanol yielded in components with two different appearances. Specifically, (2a-b) shows a shimmery catalyst surface with probably a good nickel dispersion, whereas (3a-b) features a rough surface with some light nickel particles visible on the surface.

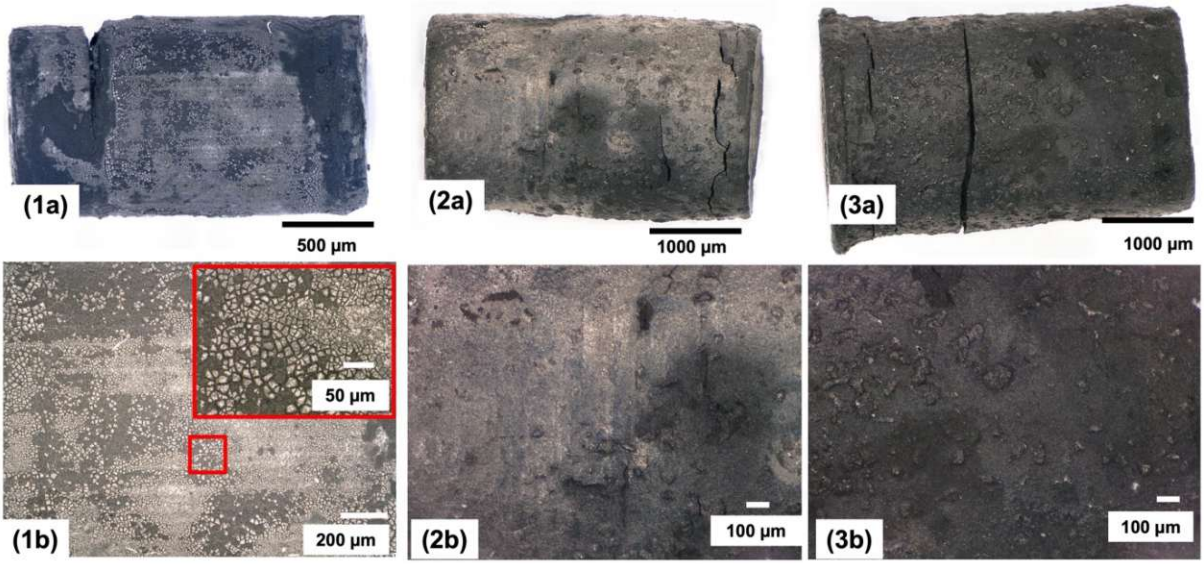

Figure 27: 3D-microscope images of the functionalised La-modified components; (1a-b) surface component after impregnation with nickelnickel nitrate dissolved in THF; (2a-b) and (3a-b) surface components after impregnation with nickel nitrate dissolved in ethanol

5.3.4 Interaction of Catalyst with CO_2

Figure 28 depicts the results of the CO_2-TPD measurements carried out to assess the surface basicity of both the unmodified and La-modified catalysts. The desorption curves are similar, but the La-modified sample showed a lower CO_2 desorption temperature compared to the unmodified sample, approximately 300 °C and 390 °C, respectively. These findings indicate that both catalysts possess a surface with a medium basicity, corresponding to a medium CO_2 adsorption strength.

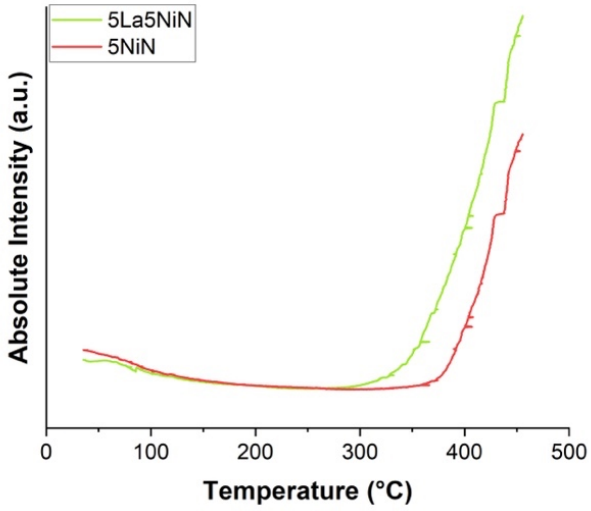

Figure 28: Comparison of the CO_2 TPD measurements of the functionalised unmodified catalyst with 5 wt% nickel to the La-modified catalyst with 5 wt% nickel (THF solvent)

5.3.5 Accessibility of Nickel

Figure 29 displays the temporal evolution of CO adsorption in the vacuum cell in five-minute intervals. Additionally, it also shows the IR spectra after CO adsorption, upon readjusting the pressure back to vacuum. The band at 2058 cm^{-1} exhibits a slight increase during the adsorption process. Conversely, the La-modified sample displays an IR band at 2038 cm^{-1} after CO adsorption, in contrast to the unmodified sample. The CO desorption occurred at approximately 100 °C. These observations suggest that CO is again linearly bonded to the nickel particles, but the interaction with CO is noticeably stronger.

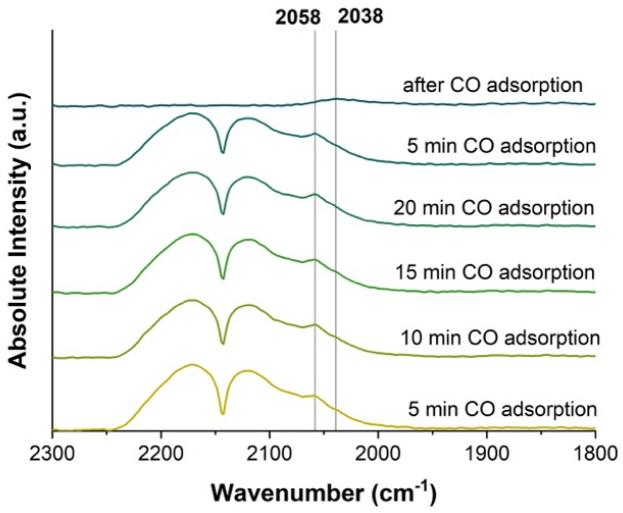

Figure 29: IR spectra of CO adsorption on La-modified catalyst with 5 wt% Nickel (THF) at different times of adsorption

5.3.6 Catalytic Performance

Figure 30 depicts the results of the catalytic tests for the La-modified catalysts that were prepared with the nickel nitrate precursor and varying solvents, in comparison to the unmodified catalyst with

5 wt% nickel prepared with method 1. The La-modified component impregnated with method 3 (THF) exhibited considerably low CO_2 conversions, with a maximum of 11 % at 400 °C. Conversely, the catalyst prepared with method 4 (EtOH) demonstrated higher CO_2 conversions, particularly at lower temperatures. Specifically, the CO_2 conversion at 350 °C with 52 % was 14 % higher compared to the unmodified catalyst. However, at 400 °C the unmodified catalyst achieved a higher CO_2 conversion with 67 %, whereas the La-modified catalyst only achieved 60 % CO_2 conversion. It is noteworthy that the CH_4 selectivity for all samples remained constant at 100% for all temperatures.

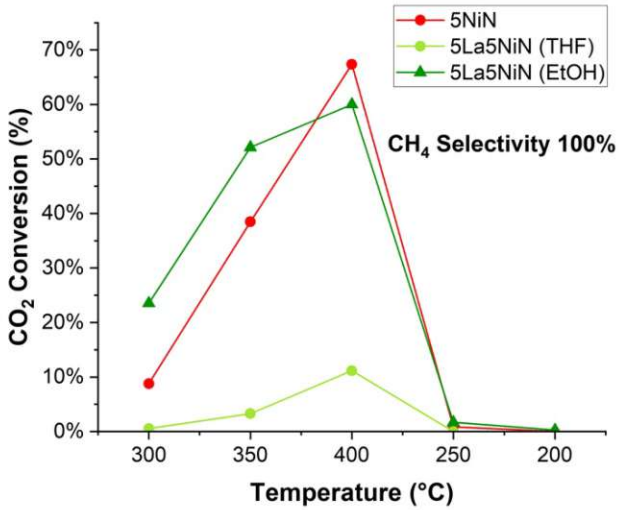

Figure 30: Comparison of the CO_2 conversion of the unmodified catalyst with 5 wt% nickel (red) and the La-modified catalysts with 5 wt% nickel (green)

5.4 Catalyst Geometry Optimisation

The previous investigations on catalysts in this project solely focused on the preparation of cylindrical shapes. As Johannes Eßmeister had already successfully 3D-printed complex shapes during his PhD-thesis, the objective of this section of this thesis was to optimize the geometry of the catalyst by printing and functionalizing a complex structure that would accurately fit into the steel reactor where the catalytic activity is evaluated.

5.4.1 Upscaling of Catalyst Preparation

The production of complex structures, particularly during pyrolysis, posed several challenges. Firstly, increasing the batch size from 10 g to 40 g of resin to print enough material for catalytic applications using a larger printing platform was difficult, especially when printing grid structures. In this case, the top layer of the grid structure tended to adhere to the FEP foil of the resin tank, the first layer tended to slightly over-polymerize and stick to the primer layer of the building platform. Secondly, the shrinkage after pyrolysis was found to be severely anisotropic. Figure 31 (1a-b) depicts the green body of a 13 mm diameter grid structure, while Figure 31 (2a-c) shows the pyrolyzed grid structure with clear anisotropy. Further, the side of the structure facing the bottom during pyrolysis experienced much higher shrinkage compared to the top side.

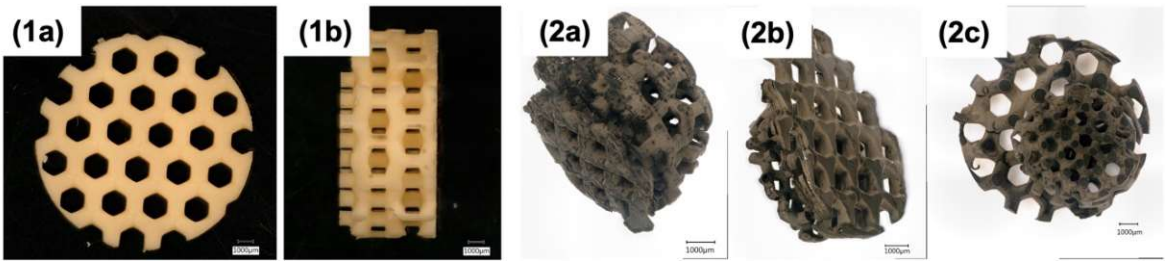

Figure 31: (1a-b) green body of the grid structure with a diameter of 13 mm: (1a) top view; (2b) side view; (2a-c) pyrolyzed grid structure: (2a-b) side view in different angles; (2c) top view

Given the delicate nature of the grid structure, particularly for the green bodies, gyroids were the chosen geometry for the catalytic application. The diameter was reduced to 9 mm and the hight was adjusted to 14 mm, as depicted in Figure 32 (1). To mitigate anisotropic shrinkage and attain catalysts of the appropriate dimensions for the steel reactor tube, the bottom third of the gyroid was removed with a razor blade and used as sacrificial material during pyrolysis to counteract the unsymmetrical shrinkage. Figure 32 (3a-b) illustrates the pyrolyzed top portion, which, again, exhibited anisotropic shrinkage. The top part featured a diameter of approximately 7 mm, while the bottom had a diameter of roughly 3,5 mm. However, the sacrificial material exhibited isotropic shrinkage, resulting in a diameter of about 3,5 mm. This poses the challenge when accounting for the diameter of the steel reactor, which is 6 mm: not all gyroids can be accommodated in the tube. Nevertheless, the gyroids were impregnated with method 1 to yield some catalytic outcome. Regrettably, only 0,4 g of gyroids could fit into the reactor, and the measurement had to be conducted with less material.

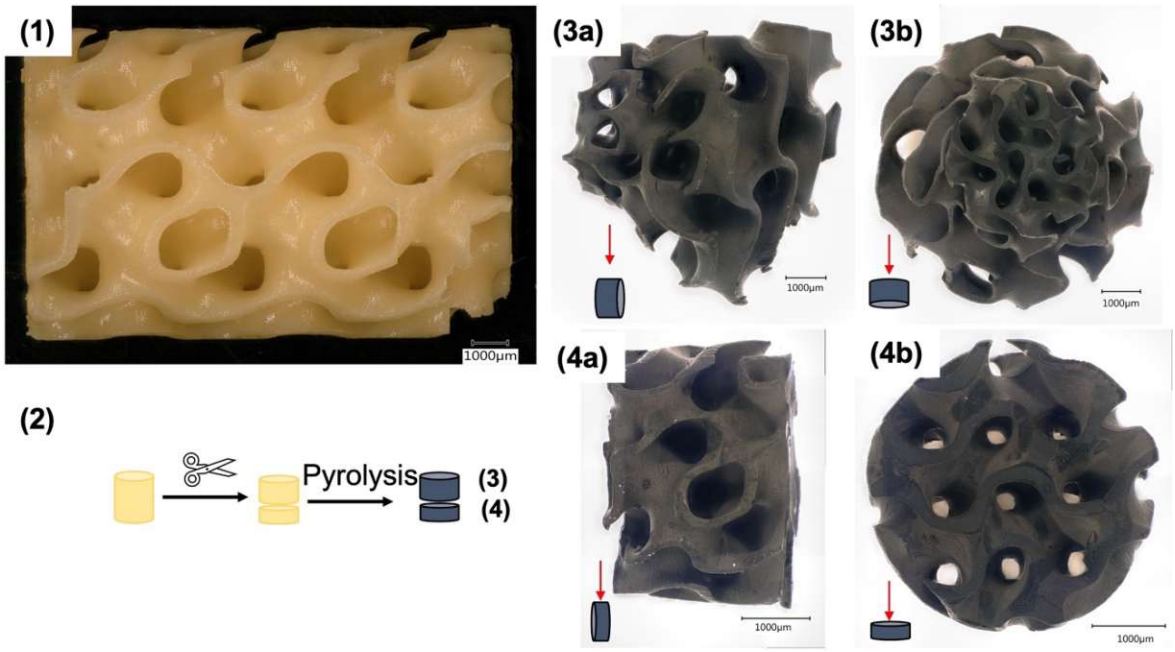

Figure 32: (1) 3-D printed green body of a gyroid structure; (2) Realisation of the preparation prior to pyrolysis, where the green body was cut and the bottom third was used as sacrificial material; (3a-b) top of the pyrolyzed structure: (a) side view; (b) top view, of the bottom (4a-b) sacrificial material: (a) side view; (b) top view

5.4.2 Catalytic Performance

The results of the catalytic performance test, as shown in Figure 33, demonstrate that the impregnated gyroid structures outperformed the cylinders. Remarkably, despite using less material for the test (0,4 g instead of 0,5 g), the gyroid structures exhibited a higher catalytic activity, with a maximum CO_2 conversion of 74 % at 400 °C.

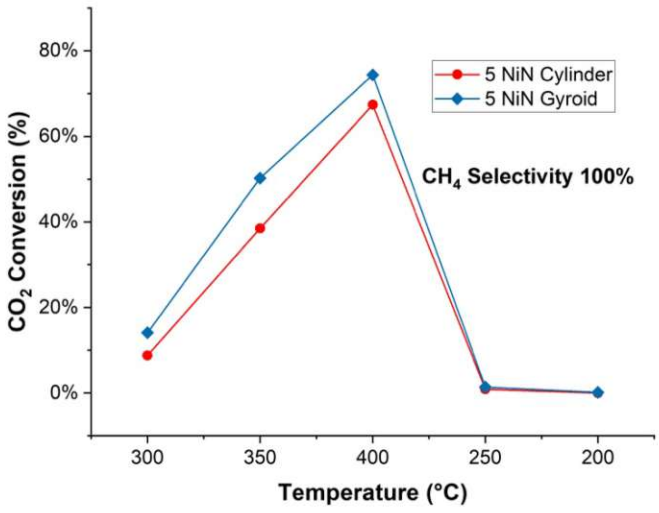

Figure 33: Comparison of the catalytic performance of the cylinder (red) and the gyroid (blue) with 5 wt% nickel

5.5 In-Situ Functionalisation

The catalysts utilized in this section were prepared by Johannes Eßmeister, while the author of this thesis evaluated their catalytic performance. Additionally, Johannes Eßmeister conducted further characterisations, including XRD, BET and elemental analysis.

5.5.1 Catalytic Performance

5.5.1.1 Effect of nickel loading and pyrolysis temperature

Figure 34 not only depicts the impact of nickel loading and pyrolysis temperature on the catalytic activity of 3D printed in-situ functionalised cylinders compared to ground powder, but also evaluates the influence of the choice of desktop printer. It can be observed that cylinders in-situ functionalised with 5 wt% nickel exhibited poor catalytic activity, with a negligible CH_4 selectivity. The ground powder of cylinders printed with the Elegoo desktop printer presented the highest CO_2 conversion rates, with a methane selectivity of 56 %. Further, increasing the nickel loading to 20 wt% did not improve the CO_2 conversion when pyrolyzing the green bodies with the same temperature profile. Notably, reducing the pyrolysis temperature from 700 °C to 600 °C significantly increased the CO_2 conversion rate, particularly for the ground cylinders, where the maximum CO_2 conversion of 26 % was achieved at a reaction temperature of 400 °C.

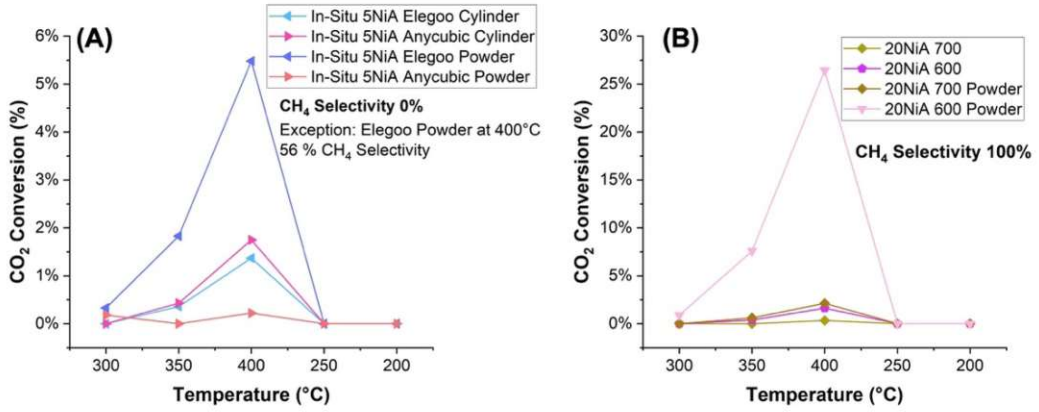

Figure 34: (A) Influence of the used desktop printer on the catalytic activity of the in-situ functionalised components with 5 wt% Ni; (B) Influence of the pyrolysis temperature on the in-situ functionalised components with 20 wt% Ni; In both graphs the cylinders were grinded to powder to make the nickel particles more accessible.

5.5.1.2 Effect of post-pyrolysis treatment

Johannes Eßmeister's basic characterisations like XRD, SEM or BET demonstrated not only a good distribution of nickel particles and small crystallite sizes of metallic nickel, but also high specific surface areas, which ought to be the ideal conditions for a high catalytic activity. However, the inaccessibility of the active phase prompted post-pyrolysis treatments to be conducted, including etching the catalyst with NaOH and evaporating excess solvent utilizing a freeze dryer. Despite these measures, the CO_2 conversions remained negligible, as seen in Figure 35.

Nonetheless, exposing the pyrolyzed cylinders to an oxidizing atmosphere at 440 °C resulted in excellent CO_2 conversions, with a maximum CO_2 conversion of 64 % achieved at 400 °C. Figure 35 (B) shows the comparison of the cylinders with 20 wt% nickel and the distinct improvement in CO_2 conversion after performing the oxidizing treatment. To evaluate the stability of the component, the catalytic activity was tested for 50 hours at 400 °C. As shown in Figure 35 (C), only a minor decrease in CO_2 conversion was observed.

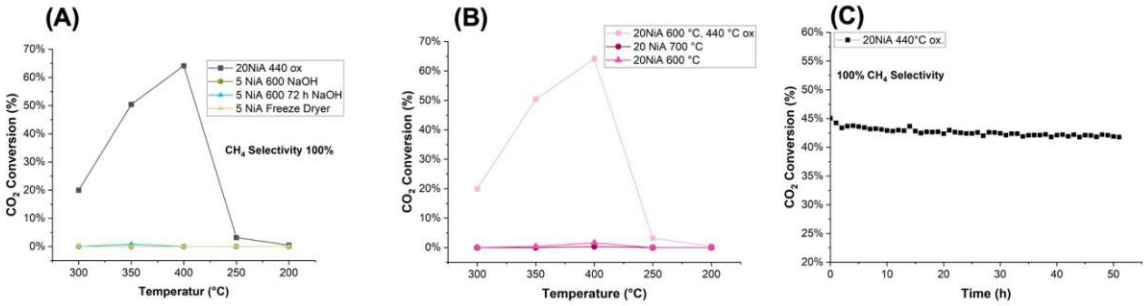

Figure 35: (A) Results of catalytic tests of in-situ functionalised samples after various post pyrolysis treatments; (B) comparison of the CO_2 conversion of the in-situ functionalised cylinders with 20 wt% nickel prior and after an oxidizing treatment; (C) Stability test of the catalyst with 20 wt% nickel after the oxidizing treatment

5.5.2 Investigation of the effect of the post-pyrolysis treatment

Powder diffraction patterns were collected to investigate the effects of the oxidizing treatment on the sample with 20 wt% nickel pyrolyzed at 600 °C. The outcomes revealed a pure nickel phase in the oxidized catalysts, whereas the untreated sample showed a reflex at 26 °Θ, indicating the presence of excess carbon. It can be concluded that the oxidizing treatment may have resulted in the removal of some of the carbon.

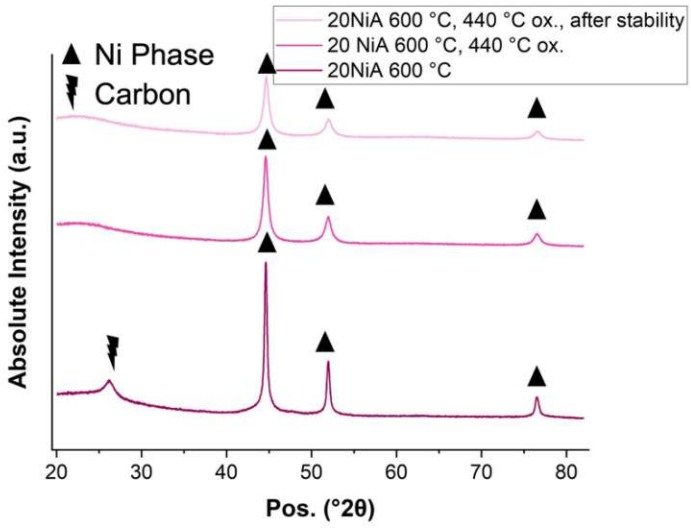

Figure 36: Comparison of powder diffractograms of the in-situ functionalised catalysts with 20 wt% nickel pyrolyzed at 600 °C, before the oxidizing treatment, after the oxidizing treatment, and after the stability test

Moreover, the crystallite size of the catalyst remained relatively constant before and after the stability test. However, it is worth noting that the catalyst without oxidizing treatment exhibited a crystallite size approximately twice as large as the other samples, as shown in Table 10.

Table 10: Crystallite size of the in-situ functionalised catalysts with 20 wt%

Sample Description	Crystallite Size (nm)
20NiA, 600 °C	21,8
20NiA, 600 °C, 440 °C ox.	11,9
20NiA, 600 °C, 440 °C ox., after stability test	10,8

BET measurements were performed to investigate changes in specific surface area, pore size distribution and N_2-adsorption-desorption-isotherms. The untreated catalyst showed a type II isotherm with a small hysteresis, while the oxidized catalyst exhibited a type IV isotherm with a more pronounced hysteresis, indicating the presence of mesopores. This assumption was further corroborated by the BJH pore size distribution, where a peak at approximately 10 nm confirmed the presence of mesopores. The juxtaposition of the sorption isotherms is given in Figure 37.

The comparisons of the BET specific surface area demonstrated only a minor difference between the untreated and oxidized catalyst, with specific surface areas of 330 $m^2 g^{-1}$ and 322 $m^2 g^{-1}$, respectively. Additionally, the untreated catalyst exhibited a BJH average pore size of 3,8 nm, while the oxidized catalyst featured a slightly higher average pore size of 5,8 nm.

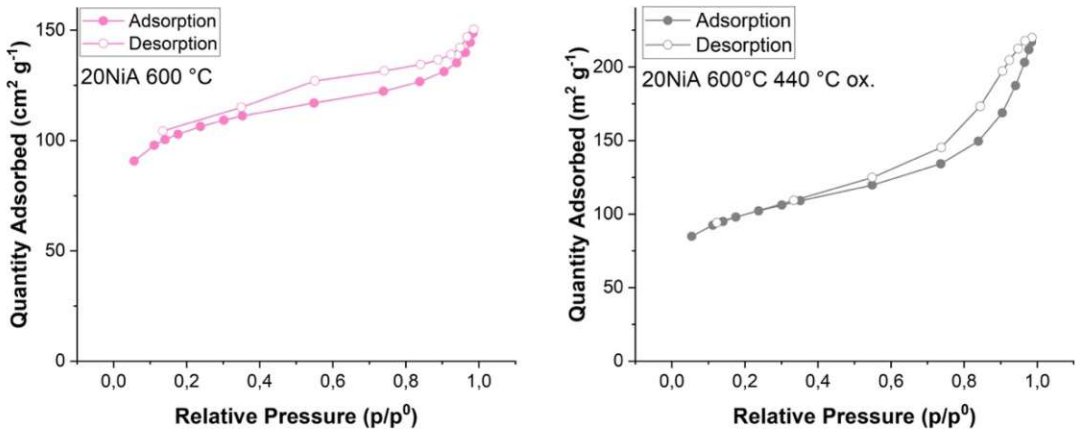

Figure 37: Comparison of the N_2-adsorption-desorption isotherms of the in-situ functionalised PDC with 20 wt% Ni pyrolyzed at 600 °C (left) and of the in-situ functionalised PDC with 20 wt% Ni pyrolyzed at 600 °C with an oxidizing treatment at 440 °C after pyrolysis (right)

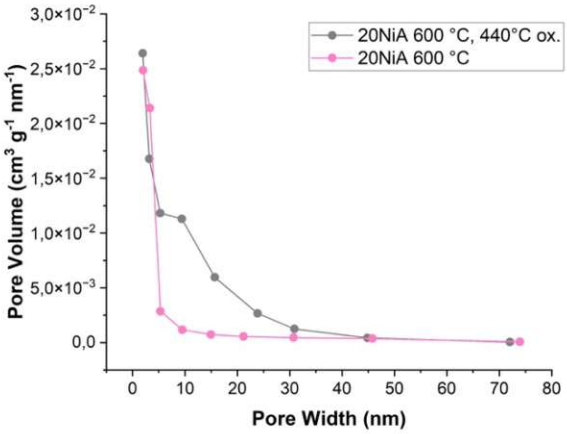

Figure 38: BJH pore Size distribution of the La-modified catalyst compared to the unmodified catalyst

Given the presence of a carbon reflex alongside the normal nickel pattern in the XRD data, an elemental analysis was carried out to investigate possible changes in elemental compositions. The analysis was conducted utilizing the combustion method, a technique in which the sample is combusted, and the resulting CO_2 is measured. For that a LECO (Laboratory Equipment Corporation) CS230 for carbon analysis and a LECO TC400 for oxygen analysis was employed. Table 11 presents the results of the analysis, revealing a significant difference in carbon content. While the untreated catalyst contained 29 wt% carbon, the carbon content of the oxidised catalyst was reduced to 12,5 wt%.

Table 11: Elemental analysis with the combustion method of the in-situ functionalised catalyst with 20 wt% nickel pyrolyzed at 600 °C compared to the catalyst oxidized at 440 °C

Sample	C (wt.%)	O (wt%)	Si + Ni (wt.%)
20NiA 600 °C	29,0 +/- 0,5	28 +/- 2,0	43,0
20NiA 600°C, 440 °C ox.	12,5 +/- 0,1	32,4 +/- 2,7	32,6

6 Discussion

6.1 Impregnation Functionalisation

6.1.1 Impregnation Functionalisation on Unmodified SiOC Support

The importance of the catalyst support on the overall catalytic performance cannot be understated. Numerous studies have demonstrated that a high specific surface area, when combined with open, hierarchical porosity, is desirable for enhancing the dispersion of the active phase.[46] In addition, the tailoring of the surface basicity has a significant effect on CO_2 adsorption capacity and, consequently, the overall CO_2 methanation performance.[32]

During Eva Szoldatits' diploma thesis, 3D printed SiOC components were manufactured and ground to a powder. The results demonstrated that the BET specific surface area was significantly influenced by the pyrolysis temperature. Specifically, for the unfunctionalized powder, a pyrolysis temperature of 600 °C reached a specific surface area of 366 $m^2 g^{-1}$, whereas the pyrolysis at 800 °C resulted in only 90 $m^2 g^{-1}$. Furthermore, catalytic tests achieved a CO_2 conversion of 44 % and 61,6 % for the the catalysts impregnated with 5 wt% nickel and pyrolyzed at 800 °C and 600 °C, respectively. However, in contrast to the impregnated cylinders manufactured in this thesis, the cylinders in Szoldatits' work were ground to a powder prior to impregnation due to the poor adhesion and dispersion of the nickel precursor on the support during the impregnation of the printed components.[47] Therefore, this thesis presented a novel impregnation technique for the functionalisation of structures produced by additive manufacturing as CO_2 methanation catalysts.

Through the utilization of the newly developed phase-separating resin for additive manufacturing of cylindrical and complex shaped components, high BET specific surface areas were achieved in the 3D printed cylinders. Specifically, the unfunctionalized components exhibited a BET specific surface area of 249 $m^2 g^{-1}$, while the nickel functionalised cylinders, prepared via the impregnation route, had BET specific surface areas ranging between 134 $m^2 g^{-1}$ and 196 $m^2 g^{-1}$. In addition, it was observed that the BET specific surface area was influenced by the impregnation technique used. Notably, the catalyst prepared with 10 wt% nickel in two consecutive steps of 5 wt% nickel exhibited the highest specific surface area. Conversely, the catalyst prepared using 10 wt% of nickel in one step showed the lowest specific surface area. The trend of the specific surface area for the different nickel loadings was as follows: 10NiN1 > 5NiN > 15NiN > 10NiN2.

Moreover, the high specific surface area and porous structure of the printed components might have had a favourable impact on the dispersion of the nickel precursor when using the impregnation method 1. Evidence supporting this hypothesis was found through SEM image examination and CO adsorption experiments, but particularly through analysis of high-magnification BSE images. These images highlighted the presence of finely dispersed nickel particles within the porous structure of

the support material. Furthermore, the detection of the IR band at 2058 cm^{-1} provides an indication for the existence of small and finely dispersed nickel particles, as the region from 2000 cm^{-1} to 2100 cm^{-1} corresponds to the stretching vibration of linearly bonded CO.[54]

The performance of CO_2 conversion was found to be impacted by the nickel loading. It was observed that, although the CO_2 conversion was comparable for all catalysts at 400 °C, the CO_2 conversion improved at lower temperatures, particularly at 350 °C, for the catalysts with 10 wt% and 15 wt% nickel. Catalytic activity at 350 °C increased as follows: 5NiN < 10NiN2 < 10NiN1 < 15NiN. This trend is consistent with existing literature data from Aziz et al., which compared the effects of different nickel loadings on mesostructured silica nanoparticles. Additionally, the catalytic tests of the study by Aziz et al. demonstrated a methane selectivity of 100%. The authors suggested that this finding may be attributed to the existence of a nickel phase within the bulk of the material.[55] This proposition could also account for the high methane selectivity attained in the catalytic tests carried out for this thesis, given the presence of nickel particles in the material's bulk, as revealed in the SEM BSE images of the fracture surface. Another possible explanation for the observed higher CO_2 conversion at lower temperatures is to examine the CO_2 TPD results. Specifically, the 5NiN catalyst exhibited CO_2 desorption beginning at around 390 °C, while the 10NiN and 15NiN catalysts exhibited CO_2 desorption initiated at around 350 °C. This finding supports the proposal put forth by Aziz et al. that the balance between nickel and basic site concentration is crucial for the CO_2 methanation activity.[55]

6.1.2 Impregnation Functionalisation on La-modified SiOC Support

The phase-separating resin employed for the manufacturing of 3D printed cylindrical components to achieve a porous SiOC material with a high specific surface area was in-situ modified with lanthanum(III) acetylacetonate. The XRD data of the La-modified support revealed an amorphous phase, indicating that lanthanum was integrated in the SiOC matrix. Hence, lanthanum was not reduced and likely existed in its oxidic state. This observation is significant and provides insight into the behaviour of the La-modified SiOC matrix. Specifically, this finding may explain why the impregnation method 1, which utilized THF as the solvent for the nickel precursor, did not yield the desired outcome. Instead, a more polar solvent like ethanol was required to achieve even distribution of the nickel particles on the catalyst surface.

A study by Wierzbicki et al. examined the impact of the La promotion on nickel-containing hydrotalcite-derived catalysts. The authors observed that the La-modification resulted in an increased catalyst activity, which they attributed to an increase in the population of medium basic sites.[53] Furthermore, it is worth noting that the presence of lanthanum had a noticeable effect on the interaction of nickel with the hydrotalcite matrix, resulting in small and well dispersed nickel crystallites.[56] Moreover, Garbarino et al. conducted a study that yielded similar insightful findings. They found that the addition of lanthanum to Ni/Al_2O_3 catalysts increased the activity of CO_2

methanation in the temperature range from 250 °C to 350 °C, an effect ascribed to the stronger basicity of the La-alumina support induced by the lanthanum.[57]

The findings of this thesis demonstrate a consistent trend with previous literature, where CO_2 conversion increases at lower temperatures, particularly at 350 °C for the La-modified catalyst. Although a complete CO_2 desorption profile was not measured, the results align with literature data, where an increased number of medium basic sites and the total basicity was estimated from the area of the CO_2 desorption peaks.[53] In comparison to the unmodified catalyst, the lanthanum-modified catalyst exhibited a lower temperature for CO_2 desorption initiation (around 300 °C) and a higher intensity of the CO_2 peak, implying an increase in the amount of medium basic sites for the La-promoted catalyst.

The results of the CO adsorption experiments suggest that the accessibility of the nickel particles on the La-modified support is similar to that of the unmodified catalyst, as indicated by the IR band at 2058 cm^{-1} observed in both samples. However, the interaction between CO and nickel particles is expected to be stronger in the La-modified sample, given that CO did not immediately desorb after vacuum readjustment, but merely resulted in a shift of the IR band to 2038 cm^{-1}.

6.1.3 Impregnation Functionalisation on Optimized Catalyst Geometry

In the field of methanation catalysts, fixed bed reactors, particularly packed bed reactors, are widely employed due to their simplicity and cost-effectiveness. However, uneven distribution of catalysts within the fixed bed reactors can impede uniform access of reactant gases to the catalytic surface, resulting in unexpected hotspots which further leads to nickel particle sintering and catalyst deactivation. To overcome these issues, a promising strategy is to utilize structured catalysts with high thermal conductivity, which can enhance the overall heat transfer performance. A review conducted by Huynh and Yu examined the impact of structured catalysts on CO_2 conversion. The study compared various monolithic honeycomb structured catalysts as well as 3D printed structured catalysts to powder-type and pellet-form catalysts. Results showed that both structured catalysts demonstrated higher CO_2 conversions than the latter.[58] The present study evaluated the catalytic performance of gyroid structures manufactured by 3D printing and functionalised with 5 wt% nickel via method 1. Despite using less catalyst material with imperfect geometries, the gyroid structures showed higher CO_2 conversions than the cylinders using the same total gas flow. This finding provides an indication for the promising potential of 3D printing of complex shapes combined in the fields of chemical engineering and catalyst manufacturing.

6.2 In-Situ Functionalisation

Previous studies conducted by Johannes Eßmeister et al. revealed a relatively low BET specific surface area of 132 $m^2 g^{-1}$ in the printed SiOC components without functionalisation. Furthermore, the specific surface areas were even lower for the nickel functionalised SiOC support with a BET specific surface area of 84,5 $m^2 g^{-1}$ for the sample pyrolyzed at 600 °C and only 1,6 $m^2 g^{-1}$ for the catalyst pyrolyzed at 800 °C. The low specific surface area of the printed components also manifested in their CO_2 conversion performance, which was observed to be very low, ranging from 0% to 3,5 % for the samples pyrolyzed at 800 °C and 600 °C, respectively. However, when samples were ground into a powder, a maximum CO_2 conversion of 25,6 % was achieved at the highest reaction temperature. The author ascribed the poor CO_2 conversion results to the inaccessibility of the metal centres in the printed components, as the coverage of the active site with a dense surface layer prevented access.[41]

During this work, similar problems emerged, where nickel appeared to be inaccessible due to the low catalytic activity, despite the specific surface area being significantly higher at 330 $m^2 g^{-1}$ for the sample with 20 wt% nickel. Moreover, it was observed that the conversion of CO_2 was significantly influenced by the pyrolysis temperature, particularly for the ground cylinders. Catalysts pyrolyzed at 600 °C exhibited notably higher CO_2 conversions compared to those pyrolyzed at 700 °C. This phenomenon can be explained by the hydrophobic surface properties of the material pyrolyzed at 600 °C, as reported by Eßmeister et al.[41]

Figure 35(A) illustrates the various post-pyrolysis treatments performed with the goal to enhance the accessibility of the active phase. However, only the oxidizing treatment at 440 °C resulted in a significant increase in CO_2 conversion. Investigations of this effect revealed that the porous structure transformed from nonporous to mesoporous, as evidenced by the adsorption-desorption isotherms and pore size distribution. Moreover, the elemental analysis provided valuable insights into the effect of the oxidizing treatment. It was observed that the untreated catalyst exhibited 29 wt% carbon, while the carbon content was reduced to 12,5 wt% after the oxidation. Additionally, the carbon reflex in the XRD data of the untreated catalyst was eliminated. Therefore, it can be concluded that the active sites were likely covered with a carbon layer, making them inaccessible for CO_2 methanation.

7 Conclusion

The utilization of a phase-separating resin was employed to produce SiOC cylinders and gyroid structures via 3D printing. Subsequently, these structures were nickel-functionalized through an impregnation method. Specifically, the components were immersed in a solution containing a nickel precursor and exposed to an ultrasonic bath. The application of this technique in conjunction with the components featuring a high specific surface area resulted in the production of catalysts containing small and finely dispersed nickel particles. Moreover, the impregnation protocol was expanded to La-promoted supports, revealing that the more polar surface due to the incorporation of lanthanum into the SiOC matrix in its oxidic form required a solvent with greater polarity. Further, the preceramic polymer system for additive manufacturing was also in-situ functionalised by Johannes Eßmeister. The resulting catalysts for CO_2 methanation were characterised and assessed for their catalytic activity. While the catalysts prepared via impregnation exhibited substantial CO_2 conversion, the active sites were inaccessible to the in-situ modified components. However, it was discovered that an oxidizing treatment after pyrolysis could effectively remove the carbon layer on the nickel particles, making them available for CO_2 methanation. Moreover, it was demonstrated that the increase in nickel loading enhances the CO_2 conversion at lower temperatures, but also that lanthanum promotion leads to higher methane yields, particularly at 350 °C. Furthermore, this study also revealed that complex structures could be printed and impregnated, although there remains scope for reducing anisotropic shrinkage during pyrolysis. Despite utilizing less catalytic material with imperfect gyroids, the CO_2 conversion could be improved.

8 References

(1)Aziz, M. a. A.; Jalil, A. A.; Triwahyono, S.; Ahmad, A. CO_2 Methanation over Heterogeneous Catalysts: Recent Progress and Future Prospects. *Green Chem.* **2015**, *17* (5), 2647–2663. https://doi.org/10.1039/C5GC00119F.

(2)Neftel, A.; Moor, E.; Oeschger, H.; Stauffer, B. Evidence from Polar Ice Cores for the Increase in Atmospheric CO_2 in the Past Two Centuries. *Nature* **1985**, *315* (6014), 45–47. https://doi.org/10.1038/315045a0.

(3)Hashimoto, K.; Yamasaki, M.; Fujimura, K.; Matsui, T.; Izumiya, K.; Komori, M.; El-Moneim, A. A.; Akiyama, E.; Habazaki, H.; Kumagai, N.; Kawashima, A.; Asami, K. Global CO_2 Recycling—Novel Materials and Prospect for Prevention of Global Warming and Abundant Energy Supply. *Mater. Sci. Eng. A* **1999**, *267* (2), 200–206. https://doi.org/10.1016/S0921-5093(99)00092-1.

(4)Jangam, A.; Das, S.; Dewangan, N.; Hongmanorom, P.; Hui, W. M.; Kawi, S. Conversion of CO_2 to C1 Chemicals: Catalyst Design, Kinetics and Mechanism Aspects of the Reactions. *Catal. Today* **2020**, *358*, 3–29. https://doi.org/10.1016/j.cattod.2019.08.049.

(5)Mac Dowell, N.; Fennell, P. S.; Shah, N.; Maitland, G. C. The Role of CO_2 Capture and Utilization in Mitigating Climate Change. *Nat. Clim. Change* **2017**, *7* (4), 243–249. https://doi.org/10.1038/nclimate3231.

(6)Song, C. CO_2 Conversion and Utilization: An Overview. In *CO_2 Conversion and Utilization*; Song, C., Gaffney, A. F., Fujimoto, K., Eds.; American Chemical Society: Washington, DC, 2002; Vol. 809, pp 2–30. https://doi.org/10.1021/bk-2002-0809.ch001.

(7)Shukla, R.; Ranjith, P.; Haque, A.; Choi, X. A Review of Studies on CO_2 Sequestration and Caprock Integrity. *Fuel* **2010**, *89* (10), 2651–2664. https://doi.org/10.1016/j.fuel.2010.05.012.

(8)Ulmer, U.; Dingle, T.; Duchesne, P. N.; Morris, R. H.; Tavasoli, A.; Wood, T.; Ozin, G. A. Fundamentals and Applications of Photocatalytic CO_2 Methanation. *Nat. Commun.* **2019**, *10* (1), 3169. https://doi.org/10.1038/s41467-019-10996-2.

(9)Hashimoto, K.; Habazaki, H.; Yamasaki, M.; Meguro, S.; Sasaki, T.; Katagiri, H.; Matsui, T.; Fujimura, K.; Izumiya, K.; Kumagai, N.; Akiyama, E. Advanced Materials for Global Carbon Dioxide Recycling. *Mater. Sci. Eng. A* **2001**, *304–306*, 88–96. https://doi.org/10.1016/S0921-5093(00)01457-X.

(10)Lee, W. J.; Li, C.; Prajitno, H.; Yoo, J.; Patel, J.; Yang, Y.; Lim, S. Recent Trend in Thermal Catalytic Low Temperature CO_2 Methanation: A Critical Review. *Catal. Today* **2021**, *368*, 2–19. https://doi.org/10.1016/j.cattod.2020.02.017.

(11)Le, T. A.; Kim, M. S.; Lee, S. H.; Kim, T. W.; Park, E. D. CO and CO_2 Methanation over Supported Ni Catalysts. *Catal. Today* **2017**, *293–294*, 89–96. https://doi.org/10.1016/j.cattod.2016.12.036.

(12)Gao, J.; Liu, Q.; Gu, F.; Liu, B.; Zhong, Z.; Su, F. Recent Advances in Methanation Catalysts for the Production of Synthetic Natural Gas. *RSC Adv.* **2015**, *5* (29), 22759–22776. https://doi.org/10.1039/C4RA16114A.

(13)Xia, A.; Yin, J.; Chen, X.; Liu, X.; Huang, Z. Polymer-Derived Si-Based Ceramics: Recent Developments and Perspectives. *Crystals* **2020**, *10* (9), 824. https://doi.org/10.3390/cryst10090824.

(14)Alper, E.; Yuksel Orhan, O. CO_2 Utilization: Developments in Conversion Processes. *Petroleum* **2017**, *3* (1), 109–126. https://doi.org/10.1016/j.petlm.2016.11.003.

(15)Lim, X. How to Make the Most of Carbon Dioxide. *Nature* **2015**, *526* (7575), 628–631.

(16)Li, W.; Wang, H.; Jiang, X.; Zhu, J.; Liu, Z.; Guo, X.; Song, C. A Short Review of Recent Advances in CO_2 Hydrogenation to Hydrocarbons over Heterogeneous Catalysts. *RSC Adv.* **2018**, *8* (14), 7651–7669. https://doi.org/10.1039/C7RA13546G.

(17)Saeidi, S.; Najari, S.; Hessel, V.; Wilson, K.; Keil, F. J.; Concepción, P.; Suib, S. L.; Rodrigues, A. E. Recent Advances in CO_2 Hydrogenation to Value-Added Products — Current Challenges and Future Directions. *Prog. Energy Combust. Sci.* **2021**, *85*, 100905. https://doi.org/10.1016/j.pecs.2021.100905.

(18)Mebrahtu, C.; Krebs, F.; Abate, S.; Perathoner, S.; Centi, G.; Palkovits, R. Chapter 5 - CO_2 Methanation: Principles and Challenges. In *Studies in Surface Science and Catalysis*; Albonetti, S., Perathoner, S., Quadrelli, E. A., Eds.; Horizons in Sustainable Industrial Chemistry and Catalysis; Elsevier, 2019; Vol. 178, pp 85–103. https://doi.org/10.1016/B978-0-444-64127-4.00005-7.

(19)Gao, J.; Wang, Y.; Ping, Y.; Hu, D.; Xu, G.; Gu, F.; Su, F. A Thermodynamic Analysis of Methanation Reactions of Carbon Oxides for the Production of Synthetic Natural Gas. *RSC Adv.* **2012**, *2* (6), 2358–2368. https://doi.org/10.1039/C2RA00632D.

(20)Miao, B.; Ma, S. S. K.; Wang, X.; Su, H.; Chan, S. H. Catalysis Mechanisms of CO_2 and CO Methanation. *Catal. Sci. Technol.* **2016**, *6* (12), 4048–4058. https://doi.org/10.1039/C6CY00478D.

(21)Pan, Q.; Peng, J.; Wang, S.; Wang, S. In Situ FTIR Spectroscopic Study of the CO_2 Methanation Mechanism on Ni/Ce0.5Zr0.5O2. *Catal. Sci. Technol.* **2014**, *4* (2), 502–509. https://doi.org/10.1039/C3CY00868A.

(22)Aldana, P. A. U.; Ocampo, F.; Kobl, K.; Louis, B.; Thibault-Starzyk, F.; Daturi, M.; Bazin, P.; Thomas, S.; Roger, A. C. Catalytic CO2 Valorization into CH4 on Ni-Based Ceria-Zirconia. Reaction Mechanism by Operando IR Spectroscopy. *Catal. Today* **2013**, *215*, 201–207. https://doi.org/10.1016/j.cattod.2013.02.019.

(23)Westermann, A.; Azambre, B.; Bacariza, M. C.; Graça, I.; Ribeiro, M. F.; Lopes, J. M.; Henriques, C. Insight into CO_2 Methanation Mechanism over NiUSY Zeolites: An Operando IR Study. *Appl. Catal. B Environ.* **2015**, *174–175*, 120–125. https://doi.org/10.1016/j.apcatb.2015.02.026.

(24)Kattel, S.; Liu, P.; Chen, J. G. Tuning Selectivity of CO_2 Hydrogenation Reactions at the Metal/Oxide Interface. *J. Am. Chem. Soc.* **2017**, *139* (29), 9739–9754. https://doi.org/10.1021/jacs.7b05362.

(25)Younas, M.; Loong Kong, L.; Bashir, M. J. K.; Nadeem, H.; Shehzad, A.; Sethupathi, S. Recent Advancements, Fundamental Challenges, and Opportunities in Catalytic Methanation of CO_2. *Energy Fuels* **2016**, *30* (11), 8815–8831. https://doi.org/10.1021/acs.energyfuels.6b01723.

(26)Frontera, P.; Macario, A.; Ferraro, M.; Antonucci, P. Supported Catalysts for CO_2 Methanation: A Review. *Catalysts* **2017**, *7* (12), 59. https://doi.org/10.3390/catal7020059.

(27)Kuznecova, I.; Gusca, J. Property Based Ranking of CO and CO_2 Methanation Catalysts. *Energy Procedia* **2017**, *128*, 255–260. https://doi.org/10.1016/j.egypro.2017.09.068.

(28)GmbH Finanzen Net. Nickelpreis, Akuteller Nickel Kurs. https://www.finanzen.net/rohstoffe/nickelpreis/forwardcurve (accessed 2023-05-19).

(29)Gold.de, Ruthenium Preis. https://www.gold.de/kurse/rutheniumpreis/ (accessed 2023-05-19).

(30)Mohd Ridzuan, N. D.; Shaharun, M. S.; Anawar, M. A.; Ud-Din, I. Ni-Based Catalyst for Carbon Dioxide Methanation: A Review on Performance and Progress. *Catalysts* **2022**, *12* (5), 469. https://doi.org/10.3390/catal12050469.

(31)Forzatti, P.; Lietti, L. Catalyst Deactivation. *Catal. Today* **1999**, *52* (2), 165–181. https://doi.org/10.1016/S0920-5861(99)00074-7.

(32)Shen, L.; Xu, J.; Zhu, M.; Han, Y.-F. Essential Role of the Support for Nickel-Based CO_2 Methanation Catalysts. *ACS Catal.* **2020**, *10* (24), 14581–14591. https://doi.org/10.1021/acscatal.0c03471.

(33)Ewald, S.; Kolbeck, M.; Kratky, T.; Wolf, M.; Hinrichsen, O. On the Deactivation of Ni-Al Catalysts in CO_2 Methanation. *Appl. Catal. Gen.* **2019**, *570*, 376–386. https://doi.org/10.1016/j.apcata.2018.10.033.

(34)Gonçalves, L. P. L.; Mielby, J.; Soares, O. S. G. P.; Sousa, J. P. S.; Petrovykh, D. Y.; Lebedev, O. I.; Pereira, M. F. R.; Kegnæs, S.; Kolen'ko, Y. V. In Situ Investigation of the CO_2 Methanation on Carbon/Ceria-Supported Ni Catalysts Using Modulation-Excitation DRIFTS. *Appl. Catal. B Environ.* **2022**, *312*, 121376. https://doi.org/10.1016/j.apcatb.2022.121376.

(35)Hu, F.; Ye, R.; Lu, Z.-H.; Zhang, R.; Feng, G. Structure–Activity Relationship of Ni-Based Catalysts toward CO_2 Methanation: Recent Advances and Future Perspectives. *Energy Fuels* **2022**, *36* (1), 156–169. https://doi.org/10.1021/acs.energyfuels.1c03645.

(36)Li, J.; Lin, Y.; Pan, X.; Miao, D.; Ding, D.; Cui, Y.; Dong, J.; Bao, X. Enhanced CO_2 Methanation Activity of Ni/Anatase Catalyst by Tuning Strong Metal–Support Interactions. *ACS Catal.* **2019**, *9* (7), 6342–6348. https://doi.org/10.1021/acscatal.9b00401.

(37)Muroyama, H.; Tsuda, Y.; Asakoshi, T.; Masitah, H.; Okanishi, T.; Matsui, T.; Eguchi, K. Carbon Dioxide Methanation over Ni Catalysts Supported on Various Metal Oxides. *J. Catal.* **2016**, *343*, 178–184. https://doi.org/10.1016/j.jcat.2016.07.018.

(38)Aziz, M. A. A.; Jalil, A. A.; Triwahyono, S.; Mukti, R. R.; Taufiq-Yap, Y. H.; Sazegar, M. R. Highly Active Ni-Promoted Mesostructured Silica Nanoparticles for CO_2 Methanation. *Appl. Catal. B Environ.* **2014**, *147*, 359–368. https://doi.org/10.1016/j.apcatb.2013.09.015.

(39)Colombo, P.; Mera, G.; Riedel, R.; Sorarù, G. D. Polymer-Derived Ceramics: 40 Years of Research and Innovation in Advanced Ceramics. In *Ceramics Science and Technology*; Riedel, R., Chen, I.-W., Eds.; Wiley-VCH Verlag GmbH & Co. KGaA: Weinheim, Germany, 2013; pp 245–320. https://doi.org/10.1002/9783527631971.ch07.

(40)Liu, J.; Tian, C.; Jiang, T.; Ricohermoso, E. I.; Yu, Z.; Ionescu, E.; Molina-Luna, L.; Hofmann, J. P.; Riedel, R. Polymer-Derived SiOC Ceramics: A Potential Catalyst Support Controlled by the Sintering Temperature and Carbon Content. *J. Eur. Ceram. Soc.* **2023**. https://doi.org/10.1016/j.jeurceramsoc.2023.02.045.

(41)Essmeister, J.; Altun, A. A.; Staudacher, M.; Lube, T.; Schwentenwein, M.; Konegger, T. Stereolithography-Based Additive Manufacturing of Polymer-Derived SiOC/SiC Ceramic Composites. *J. Eur. Ceram. Soc.* **2022**, *42* (13), 5343–5354. https://doi.org/10.1016/j.jeurceramsoc.2022.06.021.

(42)Chaudhary, R. P.; Parameswaran, C.; Idrees, M.; Rasaki, A. S.; Liu, C.; Chen, Z.; Colombo, P. Additive Manufacturing of Polymer-Derived Ceramics: Materials, Technologies, Properties and Potential Applications. *Prog. Mater. Sci.* **2022**, *128*, 100969. https://doi.org/10.1016/j.pmatsci.2022.100969.

(43)Yang, N. Fundamental Understanding and Functionality of Silicon Oxycarbide, Virginia Tech, 2021. https://vtechworks.lib.vt.edu/handle/10919/101789 (accessed 2023-03-03).

(44)Zakeri, S.; Vippola, M.; Levänen, E. A Comprehensive Review of the Photopolymerization of Ceramic Resins Used in Stereolithography. *Addit. Manuf.* **2020**, *35*, 101177. https://doi.org/10.1016/j.addma.2020.101177.

(45)Rasaki, S. A.; Xiong, D.; Xiong, S.; Su, F.; Idrees, M.; Chen, Z. Photopolymerization-Based Additive Manufacturing of Ceramics: A Systematic Review. *J. Adv. Ceram.* **2021**, *10* (3), 442–471. https://doi.org/10.1007/s40145-021-0468-z.

(46)Macedo, H. P.; Medeiros, R. L. B. A.; Ilsemann, J.; Melo, D. M. A.; Rezwan, K.; Wilhelm, M. Nickel-Containing Hybrid Ceramics Derived from Polysiloxanes with Hierarchical Porosity for CO_2 Methanation. *Microporous Mesoporous Mater.* **2019**, *278*, 156–166. https://doi.org/10.1016/j.micromeso.2018.11.006.

(47)Szoldatits, E. M. Catalytic Properties of Functionalized Polymer-Derived Ceramics Prepared by Additive Manufacturing (Masterthesis), Vienna University of Technology, 2022. https://repositum.tuwien.at/handle/20.500.12708/80593 (accessed 2023-03-09).

(48)Moore, D. G.; Barbera, L.; Masania, K.; Studart, A. R. Three-Dimensional Printing of Multicomponent Glasses Using Phase-Separating Resins. *Nat. Mater.* **2020**, *19* (2), 212–217. https://doi.org/10.1038/s41563-019-0525-y.

(49)Fuchsberger, A.-M. Polymer-Derived Ceramics with Hierarchical Porosity by Phase Separation (not published, Masterthesis) Vienna University of Technology, Vienna.

(50)ALOthman, Z. A Review: Fundamental Aspects of Silicate Mesoporous Materials. *Materials* **2012**, *5* (12), 2874–2902. https://doi.org/10.3390/ma5122874.

(51)Bardestani, R.; Patience, G. S.; Kaliaguine, S. Experimental Methods in Chemical Engineering: Specific Surface Area and Pore Size Distribution Measurements—BET, BJH, and DFT. *Can. J. Chem. Eng.* **2019**, *97* (11), 2781–2791. https://doi.org/10.1002/cjce.23632.

(52)Liebau, F. Ordered Microporous and Mesoporous Materials with Inorganic Hosts: Definitions of Terms, Formula Notation, and Systematic Classification. *Microporous Mesoporous Mater.* **2003**, *58* (1), 15–72. https://doi.org/10.1016/S1387-1811(02)00546-2.

(53)Wierzbicki, D.; Baran, R.; Dębek, R.; Motak, M.; Gálvez, M. E.; Grzybek, T.; Da Costa, P.; Glatzel, P. Examination of the Influence of La Promotion on Ni State in Hydrotalcite-Derived Catalysts under CO_2 Methanation Reaction Conditions: Operando X-Ray Absorption and Emission Spectroscopy Investigation. *Appl. Catal. B Environ.* **2018**, *232*, 409–419. https://doi.org/10.1016/j.apcatb.2018.03.089.

(54)Primet, M. Adsorption of CO on Well-Defined Ni/SiO_2 Catalysts in the 195-373 K Range Studied by Infrared Spectroscopy and Magnetic Methods. *J. Catal.* **1977**, *46* (1), 25–36. https://doi.org/10.1016/0021-9517(77)90132-4.

(55)Aziz, M. A. A.; Jalil, A. A.; Triwahyono, S.; Saad, M. W. A. CO_2 Methanation over Ni-Promoted Mesostructured Silica Nanoparticles: Influence of Ni Loading and Water Vapor on Activity and Response Surface Methodology Studies. *Chem. Eng. J.* **2015**, *260*, 757–764. https://doi.org/10.1016/j.cej.2014.09.031.

(56)Wierzbicki, D.; Motak, M.; Grzybek, T.; Gálvez, M. E.; Da Costa, P. The Influence of Lanthanum Incorporation Method on the Performance of Nickel-Containing Hydrotalcite-Derived Catalysts in CO_2 Methanation Reaction. *Catal. Today* **2018**, *307*, 205–211. https://doi.org/10.1016/j.cattod.2017.04.020.

(57)Garbarino, G.; Wang, C.; Cavattoni, T.; Finocchio, E.; Riani, P.; Flytzani-Stephanopoulos, M.; Busca, G. A Study of Ni/La-Al2O3 Catalysts: A Competitive System for CO_2 Methanation. *Appl. Catal. B Environ.* **2019**, *248*, 286–297. https://doi.org/10.1016/j.apcatb.2018.12.063.

(58)Huynh, H. L.; Yu, Z. CO_2 Methanation on Hydrotalcite-Derived Catalysts and Structured Reactors: A Review. *Energy Technol.* **2020**, *8* (5), 1901475. https://doi.org/10.1002/ente.201901475.

9 List of Abbreviations

Table 12: Abbreviations and the corresponding meaning

Abbreviation	Meaning
3D printing	Three-Dimensional printing
AM	Additive manufacturing
BET	Brunauer-Emmett-Teller method
BJH	Barrett-Joyner-Halenda (pore size distribution)
CH_4	Methane
CO	Carbon monoxide
CO_2	Carbon dioxide
FTIR	Fourier Transform Infrared Spectroscopy
H_2	Hydrogen
IR	Infrared
MSN	Mesostructured silica nanoparticles
N_2	Nitrogen
PCP	Preceramic precursor
PDC	Polymer derived ceramic
PSO	Polysiloxane
SEM	Scanning electron microscope
SiOC	Silicon oxycarbide
SMSI	Strong metal-support interaction
SNG	Synthetic natural gas
TEOS	Tetraethylorthosilicate
TMPTMA	Trimethylolpropane trimethacrylate
TPD	Temperature programmed desorption
wt%	Weight percentage
XRD	X-ray powder diffraction